All-sky search for long-duration gravitational wave transients with initial LIGO

B. P. Abbott,[1] R. Abbott,[1] T. D. Abbott,[2] M. R. Abernathy,[1] F. Acernese,[3,4] K. Ackley,[5] C. Adams,[6] T. Adams,[7] P. Addesso,[8] R. X. Adhikari,[1] V. B. Adya,[9] C. Affeldt,[9] M. Agathos,[10] K. Agatsuma,[10] N. Aggarwal,[11] O. D. Aguiar,[12] A. Ain,[13] P. Ajith,[14] B. Allen,[9,15,16] A. Allocca,[17,18] D. V. Amariutei,[5] S. B. Anderson,[1] W. G. Anderson,[15] K. Arai,[1] M. C. Araya,[1] C. C. Arceneaux,[19] J. S. Areeda,[20] N. Arnaud,[21] K. G. Arun,[22] G. Ashton,[23] M. Ast,[24] S. M. Aston,[6] P. Astone,[25] P. Aufmuth,[16] C. Aulbert,[9] S. Babak,[26] P. T. Baker,[27] F. Baldaccini,[28,29] G. Ballardin,[30] S. W. Ballmer,[31] J. C. Barayoga,[1] S. E. Barclay,[32] B. C. Barish,[1] D. Barker,[33] F. Barone,[3,4] B. Barr,[32] L. Barsotti,[11] M. Barsuglia,[34] D. Barta,[35] J. Bartlett,[33] I. Bartos,[36] R. Bassiri,[37] A. Basti,[17,18] J. C. Batch,[33] C. Baune,[9] V. Bavigadda,[30] M. Bazzan,[38,39] B. Behnke,[26] M. Bejger,[40] C. Belczynski,[41] A. S. Bell,[32] C. J. Bell,[32] B. K. Berger,[1] J. Bergman,[33] G. Bergmann,[9] C. P. L. Berry,[42] D. Bersanetti,[43,44] A. Bertolini,[10] J. Betzwieser,[6] S. Bhagwat,[31] R. Bhandare,[45] I. A. Bilenko,[46] G. Billingsley,[1] J. Birch,[6] R. Birney,[47] S. Biscans,[11] A. Bisht,[9,16] M. Bitossi,[30] C. Biwer,[31] M. A. Bizouard,[21] J. K. Blackburn,[1] C. D. Blair,[48] D. Blair,[48] R. M. Blair,[33] S. Bloemen,[10,49] O. Bock,[9] T. P. Bodiya,[11] M. Boer,[50] G. Bogaert,[50] C. Bogan,[9] A. Bohe,[26] P. Bojtos,[51] C. Bond,[42] F. Bondu,[52] R. Bonnand,[7] R. Bork,[1] V. Boschi,[18,17] S. Bose,[53,13] A. Bozzi,[30] C. Bradaschia,[18] P. R. Brady,[15] V. B. Braginsky,[46] M. Branchesi,[54,55] J. E. Brau,[56] T. Briant,[57] A. Brillet,[50] M. Brinkmann,[9] V. Brisson,[21] P. Brockill,[15] A. F. Brooks,[1] D. A. Brown,[31] D. Brown,[5] D. D. Brown,[42] N. M. Brown,[11] C. C. Buchanan,[2] A. Buikema,[11] T. Bulik,[41] H. J. Bulten,[58,10] A. Buonanno,[26,59] D. Buskulic,[7] C. Buy,[34] R. L. Byer,[37] L. Cadonati,[60] G. Cagnoli,[61] C. Cahillane,[1] J. Calderón Bustillo,[62,60] T. Callister,[1] E. Calloni,[63,4] J. B. Camp,[64] K. C. Cannon,[65] J. Cao,[66] C. D. Capano,[9] E. Capocasa,[34] F. Carbognani,[30] S. Caride,[67] J. Casanueva Diaz,[21] C. Casentini,[68,69] S. Caudill,[15] M. Cavaglià,[19] F. Cavalier,[21] R. Cavalieri,[30] G. Cella,[18] C. Cepeda,[1] L. Cerboni Baiardi,[54,55] G. Cerretani,[17,18] E. Cesarini,[68,69] R. Chakraborty,[1] T. Chalermsongsak,[1] S. J. Chamberlin,[15] M. Chan,[32] S. Chao,[70] P. Charlton,[71] E. Chassande-Mottin,[34] H. Y. Chen,[72] Y. Chen,[73] C. Cheng,[70] A. Chincarini,[44] A. Chiummo,[30] H. S. Cho,[74] M. Cho,[59] J. H. Chow,[75] N. Christensen,[76] Q. Chu,[48] S. Chua,[57] S. Chung,[48] G. Ciani,[5] F. Clara,[33] J. A. Clark,[60] F. Cleva,[50] E. Coccia,[68,77] P.-F. Cohadon,[57] A. Colla,[78,25] C. G. Collette,[79] M. Constancio, Jr.,[12] A. Conte,[78,25] L. Conti,[39] D. Cook,[33] T. R. Corbitt,[2] N. Cornish,[27] A. Corsi,[80] S. Cortese,[30] C. A. Costa,[12] M. W. Coughlin,[76] S. B. Coughlin,[81] J.-P. Coulon,[50] S. T. Countryman,[36] P. Couvares,[1] D. M. Coward,[48] M. J. Cowart,[6] D. C. Coyne,[1] R. Coyne,[80] K. Craig,[32] J. D. E. Creighton,[15] J. Cripe,[2] S. G. Crowder,[82] A. Cumming,[32] L. Cunningham,[32] E. Cuoco,[30] T. Dal Canton,[9] S. L. Danilishin,[32] S. D'Antonio,[69] K. Danzmann,[16,9] N. S. Darman,[83] V. Dattilo,[30] I. Dave,[45] H. P. Daveloza,[84] M. Davier,[21] G. S. Davies,[32] E. J. Daw,[85] R. Day,[30] D. DeBra,[37] G. Debreczeni,[35] J. Degallaix,[61] M. De Laurentis,[63,4] S. Deléglise,[57] W. Del Pozzo,[42] T. Denker,[9,16] T. Dent,[9] H. Dereli,[50] V. Dergachev,[1] R. DeRosa,[6] R. De Rosa,[63,4] R. DeSalvo,[8] S. Dhurandhar,[13] M. C. Díaz,[84] L. Di Fiore,[4] M. Di Giovanni,[78,25] A. Di Lieto,[17,18] I. Di Palma,[26,9] A. Di Virgilio,[18] G. Dojcinoski,[86] V. Dolique,[61] F. Donovan,[11] K. L. Dooley,[19] S. Doravari,[6] R. Douglas,[32] T. P. Downes,[15] M. Drago,[9,87,88] R. W. P. Drever,[1] J. C. Driggers,[33] Z. Du,[66] M. Ducrot,[7] S. E. Dwyer,[33] T. B. Edo,[85] M. C. Edwards,[76] A. Effler,[6] H.-B. Eggenstein,[9] P. Ehrens,[1] J. M. Eichholz,[5] S. S. Eikenberry,[5] W. Engels,[73] R. C. Essick,[11] T. Etzel,[1] M. Evans,[11] T. M. Evans,[6] R. Everett,[89] M. Factourovich,[36] V. Fafone,[68,69,77] H. Fair,[31] S. Fairhurst,[81] X. Fan,[66] Q. Fang,[48] S. Farinon,[44] B. Farr,[72] W. M. Farr,[42] M. Favata,[86] M. Fays,[81] H. Fehrmann,[9] M. M. Fejer,[37] I. Ferrante,[17,18] E. C. Ferreira,[12] F. Ferrini,[30] F. Fidecaro,[17,18] I. Fiori,[30] R. P. Fisher,[31] R. Flaminio,[61] M. Fletcher,[32] J.-D. Fournier,[50] S. Franco,[21] S. Frasca,[78,25] F. Frasconi,[18] Z. Frei,[51] A. Freise,[42] R. Frey,[56] V. Frey,[21] T. T. Fricke,[9] P. Fritschel,[11] V. V. Frolov,[6] P. Fulda,[5] M. Fyffe,[6] H. A. G. Gabbard,[19] J. R. Gair,[90] L. Gammaitoni,[28,29] S. G. Gaonkar,[13] F. Garufi,[63,4] A. Gatto,[34] G. Gaur,[91,92] N. Gehrels,[64] G. Gemme,[44] B. Gendre,[50] E. Genin,[30] A. Gennai,[18] J. George,[45] L. Gergely,[93] V. Germain,[7] A. Ghosh,[14] S. Ghosh,[10,49] J. A. Giaime,[2,6] K. D. Giardina,[6] A. Giazotto,[18] K. Gill,[94] A. Glaefke,[32] E. Goetz,[67] R. Goetz,[5] L. Gondan,[51] G. González,[2] J. M. Gonzalez Castro,[17,18] A. Gopakumar,[95] N. A. Gordon,[32] M. L. Gorodetsky,[46] S. E. Gossan,[1] M. Gosselin,[30] R. Gouaty,[7] C. Graef,[32] P. B. Graff,[64,59] M. Granata,[61] A. Grant,[32] S. Gras,[11] C. Gray,[33] G. Greco,[54,55] A. C. Green,[42] P. Groot,[49] H. Grote,[9] S. Grunewald,[26] G. M. Guidi,[54,55] X. Guo,[66] A. Gupta,[13] M. K. Gupta,[92] K. E. Gushwa,[1] E. K. Gustafson,[1] R. Gustafson,[67] J. J. Hacker,[20] B. R. Hall,[53] E. D. Hall,[1] G. Hammond,[32] M. Haney,[95] M. M. Hanke,[9] J. Hanks,[33] C. Hanna,[89] M. D. Hannam,[81] J. Hanson,[6] T. Hardwick,[2] J. Harms,[54,55] G. M. Harry,[96] I. W. Harry,[26] M. J. Hart,[32] M. T. Hartman,[5] C.-J. Haster,[42] K. Haughian,[32] A. Heidmann,[57] M. C. Heintze,[5,6] H. Heitmann,[50] P. Hello,[21] G. Hemming,[30] M. Hendry,[32] I. S. Heng,[32] J. Hennig,[32] A. W. Heptonstall,[1] M. Heurs,[9,16] S. Hild,[32] D. Hoak,[97] K. A. Hodge,[1] D. Hofman,[61] S. E. Hollitt,[98] K. Holt,[6] D. E. Holz,[72] P. Hopkins,[81] D. J. Hosken,[98] J. Hough,[32] E. A. Houston,[32] E. J. Howell,[48] Y. M. Hu,[32] S. Huang,[70] E. A. Huerta,[99] D. Huet,[21] B. Hughey,[94] S. Husa,[62] S. H. Huttner,[32] T. Huynh-Dinh,[6] A. Idrisy,[89] N. Indik,[9] D. R. Ingram,[33] R. Inta,[80] H. N. Isa,[32] J.-M. Isac,[57] M. Isi,[1] G. Islas,[20] T. Isogai,[11] B. R. Iyer,[14] K. Izumi,[33] T. Jacqmin,[57] H. Jang,[74] K. Jani,[60] P. Jaranowski,[100] S. Jawahar,[101] F. Jiménez-Forteza,[62] W. W. Johnson,[2] D. I. Jones,[23] R. Jones,[32] R. J. G. Jonker,[10] L. Ju,[48] K. Haris,[102] C. V. Kalaghatgi,[22] V. Kalogera,[103] S. Kandhasamy,[19] G. Kang,[74] J. B. Kanner,[1] S. Karki,[56] M. Kasprzack,[2,21,30] E. Katsavounidis,[11] W. Katzman,[6] S. Kaufer,[16] T. Kaur,[48] K. Kawabe,[33] F. Kawazoe,[9] F. Kéfélian,[50] M. S. Kehl,[65]

 © 2016 American Physical Society

D. Keitel,[9] D. B. Kelley,[31] W. Kells,[1] R. Kennedy,[85] J. S. Key,[84] A. Khalaidovski,[9] F. Y. Khalili,[46] S. Khan,[81] Z. Khan,[92] E. A. Khazanov,[104] N. Kijbunchoo,[33] C. Kim,[74] J. Kim,[105] K. Kim,[106] N. Kim,[74] N. Kim,[37] Y.-M. Kim,[105] E. J. King,[98] P. J. King,[33] D. L. Kinzel,[6] J. S. Kissel,[33] L. Kleybolte,[24] S. Klimenko,[5] S. M. Koehlenbeck,[9] K. Kokeyama,[2] S. Koley,[10] V. Kondrashov,[1] A. Kontos,[11] M. Korobko,[24] W. Z. Korth,[1] I. Kowalska,[41] D. B. Kozak,[1] V. Kringel,[9] B. Krishnan,[9] A. Królak,[107,108] C. Krueger,[16] G. Kuehn,[9] P. Kumar,[65] L. Kuo,[70] A. Kutynia,[107] B. D. Lackey,[31] M. Landry,[33] J. Lange,[109] B. Lantz,[37] P. D. Lasky,[110] A. Lazzarini,[1] C. Lazzaro,[60,39] P. Leaci,[26,78,25] S. Leavey,[32] E. Lebigot,[34,66] C. H. Lee,[105] H. K. Lee,[106] H. M. Lee,[111] K. Lee,[32] M. Leonardi,[87,88] J. R. Leong,[9] N. Leroy,[21] N. Letendre,[7] Y. Levin,[110] B. M. Levine,[33] T. G. F. Li,[1] A. Libson,[11] T. B. Littenberg,[103] N. A. Lockerbie,[101] J. Logue,[32] A. L. Lombardi,[97] J. E. Lord,[31] M. Lorenzini,[77] V. Loriette,[112] M. Lormand,[6] G. Losurdo,[55] J. D. Lough,[9,16] H. Lück,[16,9] A. P. Lundgren,[9] J. Luo,[76] R. Lynch,[11] Y. Ma,[48] T. MacDonald,[37] B. Machenschalk,[9] M. MacInnis,[11] D. M. Macleod,[2] F. Magaña-Sandoval,[31] R. M. Magee,[53] M. Mageswaran,[1] E. Majorana,[25] I. Maksimovic,[112] V. Malvezzi,[68,69] N. Man,[50] I. Mandel,[42] V. Mandic,[82] V. Mangano,[78,25,32] G. L. Mansell,[75] M. Manske,[15] M. Mantovani,[30] F. Marchesoni,[113,29] F. Marion,[7] S. Márka,[36] Z. Márka,[36] A. S. Markosyan,[37] E. Maros,[1] F. Martelli,[54,55] L. Martellini,[50] I. W. Martin,[32] R. M. Martin,[5] D. V. Martynov,[1] J. N. Marx,[1] K. Mason,[11] A. Masserot,[7] T. J. Massinger,[31] M. Masso-Reid,[32] F. Matichard,[11] L. Matone,[36] N. Mavalvala,[11] N. Mazumder,[53] G. Mazzolo,[9] R. McCarthy,[33] D. E. McClelland,[75] S. McCormick,[6] S. C. McGuire,[114] G. McIntyre,[1] J. McIver,[97] S. T. McWilliams,[99] D. Meacher,[50] G. D. Meadors,[26,9] J. Meidam,[10] A. Melatos,[83] G. Mendell,[33] D. Mendoza-Gandara,[9] R. A. Mercer,[15] M. Merzougui,[50] S. Meshkov,[1] C. Messenger,[32] C. Messick,[89] P. M. Meyers,[82] F. Mezzani,[25,78] H. Miao,[42] C. Michel,[61] H. Middleton,[42] E. E. Mikhailov,[115] L. Milano,[63,4] J. Miller,[11] M. Millhouse,[27] Y. Minenkov,[69] J. Ming,[26,9] S. Mirshekari,[116] C. Mishra,[14] S. Mitra,[13] V. P. Mitrofanov,[46] G. Mitselmakher,[5] R. Mittleman,[11] A. Moggi,[18] S. R. P. Mohapatra,[11] M. Montani,[54,55] B. C. Moore,[86] C. J. Moore,[90] D. Moraru,[33] G. Moreno,[33] S. R. Morriss,[84] K. Mossavi,[9] B. Mours,[7] C. M. Mow-Lowry,[42] C. L. Mueller,[5] G. Mueller,[5] A. W. Muir,[81] Arunava Mukherjee,[14] D. Mukherjee,[15] S. Mukherjee,[84] A. Mullavey,[6] J. Munch,[98] D. J. Murphy,[36] P. G. Murray,[32] A. Mytidis,[5] I. Nardecchia,[68,69] L. Naticchioni,[78,25] R. K. Nayak,[117] V. Necula,[5] K. Nedkova,[97] G. Nelemans,[10,49] M. Neri,[43,44] A. Neunzert,[67] G. Newton,[32] T. T. Nguyen,[75] A. B. Nielsen,[9] S. Nissanke,[49,10] A. Nitz,[31] F. Nocera,[30] D. Nolting,[6] M. E. N. Normandin,[84] L. K. Nuttall,[31] J. Oberling,[33] E. Ochsner,[15] J. O'Dell,[118] E. Oelker,[11] G. H. Ogin,[119] J. J. Oh,[120] S. H. Oh,[120] F. Ohme,[81] M. Oliver,[62] P. Oppermann,[9] Richard J. Oram,[6] B. O'Reilly,[6] R. O'Shaughnessy,[109] C. D. Ott,[73] D. J. Ottaway,[98] R. S. Ottens,[5] H. Overmier,[6] B. J. Owen,[80] A. Pai,[102] S. A. Pai,[45] J. R. Palamos,[56] O. Palashov,[104] C. Palomba,[25] A. Pal-Singh,[24] H. Pan,[70] C. Pankow,[15,103] F. Pannarale,[81] B. C. Pant,[45] F. Paoletti,[30,18] A. Paoli,[30] M. A. Papa,[26,15,9] H. R. Paris,[37] W. Parker,[6] D. Pascucci,[32] A. Pasqualetti,[30] R. Passaquieti,[17,18] D. Passuello,[18] Z. Patrick,[37] B. L. Pearlstone,[32] M. Pedraza,[1] R. Pedurand,[61] L. Pekowsky,[31] A. Pele,[6] S. Penn,[121] R. Pereira,[36] A. Perreca,[1] M. Phelps,[32] O. Piccinni,[78,25] M. Pichot,[50] F. Piergiovanni,[54,55] V. Pierro,[8] G. Pillant,[30] L. Pinard,[61] I. M. Pinto,[8] M. Pitkin,[32] R. Poggiani,[17,18] A. Post,[9] J. Powell,[32] J. Prasad,[13] V. Predoi,[81] S. S. Premachandra,[110] T. Prestegard,[82] L. R. Price,[1] M. Prijatelj,[30] M. Principe,[8] S. Privitera,[26] G. A. Prodi,[87,88] L. Prokhorov,[46] M. Punturo,[29] P. Puppo,[25] M. Pürrer,[81] H. Qi,[15] J. Qin,[48] V. Quetschke,[84] E. A. Quintero,[1] R. Quitzow-James,[56] F. J. Raab,[33] D. S. Rabeling,[75] H. Radkins,[33] P. Raffai,[51] S. Raja,[45] M. Rakhmanov,[84] P. Rapagnani,[78,25] V. Raymond,[26] M. Razzano,[17,18] V. Re,[68,69] J. Read,[20] C. M. Reed,[33] T. Regimbau,[50] L. Rei,[44] S. Reid,[47] D. H. Reitze,[1,5] H. Rew,[115] F. Ricci,[78,25] K. Riles,[67] N. A. Robertson,[1,32] R. Robie,[32] F. Robinet,[21] A. Rocchi,[69] L. Rolland,[7] J. G. Rollins,[1] V. J. Roma,[56] J. D. Romano,[84] R. Romano,[3,4] G. Romanov,[115] J. H. Romie,[6] D. Rosińska,[122,40] S. Rowan,[32] A. Rüdiger,[9] P. Ruggi,[30] K. Ryan,[33] S. Sachdev,[1] T. Sadecki,[33] L. Sadeghian,[15] M. Saleem,[102] F. Salemi,[9] A. Samajdar,[117] L. Sammut,[83] E. J. Sanchez,[1] V. Sandberg,[33] B. Sandeen,[103] J. R. Sanders,[67] B. Sassolas,[61] P. R. Saulson,[31] O. Sauter,[67] R. Savage,[33] A. Sawadsky,[16] P. Schale,[56] R. Schilling,[9,*] J. Schmidt,[9] P. Schmidt,[1,73] R. Schnabel,[24] R. M. S. Schofield,[56] A. Schönbeck,[24] E. Schreiber,[9] D. Schuette,[9,16] B. F. Schutz,[81] J. Scott,[32] S. M. Scott,[75] D. Sellers,[6] D. Sentenac,[30] V. Sequino,[68,69] A. Sergeev,[104] G. Serna,[20] Y. Setyawati,[49,10] A. Sevigny,[33] D. A. Shaddock,[75] S. Shah,[10,49] M. S. Shahriar,[103] M. Shaltev,[9] Z. Shao,[1] B. Shapiro,[37] P. Shawhan,[59] A. Sheperd,[15] D. H. Shoemaker,[11] D. M. Shoemaker,[60] K. Siellez,[50] X. Siemens,[15] D. Sigg,[33] A. D. Silva,[12] D. Simakov,[9] A. Singer,[1] L. P. Singer,[64] A. Singh,[26,9] R. Singh,[2] A. M. Sintes,[62] B. J. J. Slagmolen,[75] J. R. Smith,[20] N. D. Smith,[1] R. J. E. Smith,[1] E. J. Son,[120] B. Sorazu,[32] F. Sorrentino,[44] T. Souradeep,[13] A. K. Srivastava,[92] A. Staley,[36] M. Steinke,[9] J. Steinlechner,[32] S. Steinlechner,[32] D. Steinmeyer,[9,16] B. C. Stephens,[15] R. Stone,[84] K. A. Strain,[32] N. Straniero,[61] G. Stratta,[54,55] N. A. Strauss,[76] S. Strigin,[46] R. Sturani,[116] A. L. Stuver,[6] T. Z. Summerscales,[123] L. Sun,[83] P. J. Sutton,[81] B. L. Swinkels,[30] M. J. Szczepanczyk,[94] M. Tacca,[34] D. Talukder,[56] D. B. Tanner,[5] M. Tápai,[93] S. P. Tarabrin,[9] A. Taracchini,[26] R. Taylor,[1] T. Theeg,[9] M. P. Thirugnanasambandam,[1] E. G. Thomas,[42] M. Thomas,[6] P. Thomas,[33] K. A. Thorne,[6] K. S. Thorne,[73] E. Thrane,[110] S. Tiwari,[77] V. Tiwari,[81] C. Tomlinson,[85] M. Tonelli,[17,18] C. V. Torres,[84,*] C. I. Torrie,[1] D. Töyrä,[42] F. Travasso,[28,29] G. Traylor,[6] D. Trifirò,[19] M. C. Tringali,[87,88] L. Trozzo,[124,18] M. Tse,[11] M. Turconi,[50] D. Tuyenbayev,[84] D. Ugolini,[125] C. S. Unnikrishnan,[95] A. L. Urban,[15] S. A. Usman,[31] H. Vahlbruch,[16] G. Vajente,[1] G. Valdes,[84] N. van Bakel,[10] M. van Beuzekom,[10] J. F. J. van den Brand,[58,10] C. van den Broeck,[10] L. van der Schaaf,[10] M. V. van der Sluys,[10,49] J. V. van Heijningen,[10] A. A. van Veggel,[32] M. Vardaro,[38,39] S. Vass,[1] M. Vasúth,[35] R. Vaulin,[11]

A. Vecchio,[42] G. Vedovato,[39] J. Veitch,[42] P. J. Veitch,[98] K. Venkateswara,[126] D. Verkindt,[7] F. Vetrano,[54,55] A. Viceré,[54,55] S. Vinciguerra,[42] J.-Y. Vinet,[50] S. Vitale,[11] T. Vo,[31] H. Vocca,[28,29] C. Vorvick,[33] W. D. Vousden,[42] S. P. Vyatchanin,[46] A. R. Wade,[75] L. E. Wade,[15] M. Wade,[15] M. Walker,[2] L. Wallace,[1] S. Walsh,[15] G. Wang,[77] H. Wang,[42] M. Wang,[42] X. Wang,[66] Y. Wang,[48] R. L. Ward,[75] J. Warner,[33] M. Was,[7] B. Weaver,[33] L.-W. Wei,[50] M. Weinert,[9] A. J. Weinstein,[1] R. Weiss,[11] T. Welborn,[6] L. Wen,[48] P. Weßels,[9] T. Westphal,[9] K. Wette,[9] J. T. Whelan,[109,9] D. J. White,[85] B. F. Whiting,[5] R. D. Williams,[1] A. R. Williamson,[81] J. L. Willis,[127] B. Willke,[16,9] M. H. Wimmer,[9,16] W. Winkler,[9] C. C. Wipf,[1] H. Wittel,[9,16] G. Woan,[32] J. Worden,[33] J. L. Wright,[32] G. Wu,[6] J. Yablon,[103] W. Yam,[11] H. Yamamoto,[1] C. C. Yancey,[59] H. Yu,[11] M. Yvert,[7] A. Zadrożny,[107] L. Zangrando,[39] M. Zanolin,[94] J.-P. Zendri,[39] M. Zevin,[103] F. Zhang,[11] L. Zhang,[1] M. Zhang,[115] Y. Zhang,[109] C. Zhao,[48] M. Zhou,[103] Z. Zhou,[103] X. J. Zhu,[48] M. E. Zucker,[11] S. E. Zuraw,[97] and J. Zweizig[1]

(The LIGO Scientific Collaboration and the Virgo Collaboration)[†]

[1]*LIGO, California Institute of Technology, Pasadena, California 91125, USA*
[2]*Louisiana State University, Baton Rouge, Louisiana 70803, USA*
[3]*Università di Salerno, Fisciano, I-84084 Salerno, Italy*
[4]*INFN, Sezione di Napoli, Complesso Universitario di Monte S.Angelo, I-80126 Napoli, Italy*
[5]*University of Florida, Gainesville, Florida 32611, USA*
[6]*LIGO Livingston Observatory, Livingston, Louisiana 70754, USA*
[7]*Laboratoire d'Annecy-le-Vieux de Physique des Particules (LAPP), Université Savoie Mont Blanc, CNRS/IN2P3, F-74941 Annecy-le-Vieux, France*
[8]*University of Sannio at Benevento, I-82100 Benevento, Italy and INFN, Sezione di Napoli, I-80100 Napoli, Italy*
[9]*Albert-Einstein-Institut, Max-Planck-Institut für Gravitationsphysik, D-30167 Hannover, Germany*
[10]*Nikhef, Science Park, 1098 XG Amsterdam, Netherlands*
[11]*LIGO, Massachusetts Institute of Technology, Cambridge, Massachusetts 02139, USA*
[12]*Instituto Nacional de Pesquisas Espaciais, 12227-010 São José dos Campos, SP, Brazil*
[13]*Inter-University Centre for Astronomy and Astrophysics, Pune 411007, India*
[14]*International Centre for Theoretical Sciences, Tata Institute of Fundamental Research, Bangalore 560012, India*
[15]*University of Wisconsin-Milwaukee, Milwaukee, Wisconsin 53201, USA*
[16]*Leibniz Universität Hannover, D-30167 Hannover, Germany*
[17]*Università di Pisa, I-56127 Pisa, Italy*
[18]*INFN, Sezione di Pisa, I-56127 Pisa, Italy*
[19]*The University of Mississippi, University, Mississippi 38677, USA*
[20]*California State University Fullerton, Fullerton, California 92831, USA*
[21]*LAL, Univ Paris-Sud, CNRS/IN2P3, Orsay, France*
[22]*Chennai Mathematical Institute, Chennai, India*
[23]*University of Southampton, Southampton SO17 1BJ, United Kingdom*
[24]*Universität Hamburg, D-22761 Hamburg, Germany*
[25]*INFN, Sezione di Roma, I-00185 Roma, Italy*
[26]*Albert-Einstein-Institut, Max-Planck-Institut für Gravitationsphysik, D-14476 Potsdam-Golm, Germany*
[27]*Montana State University, Bozeman, Montana 59717, USA*
[28]*Università di Perugia, I-06123 Perugia, Italy*
[29]*INFN, Sezione di Perugia, I-06123 Perugia, Italy*
[30]*European Gravitational Observatory (EGO), I-56021 Cascina, Pisa, Italy*
[31]*Syracuse University, Syracuse, New York 13244, USA*
[32]*SUPA, University of Glasgow, Glasgow G12 8QQ, United Kingdom*
[33]*LIGO Hanford Observatory, Richland, Washington 99352, USA*
[34]*APC, AstroParticule et Cosmologie, Université Paris Diderot, CNRS/IN2P3, CEA/Irfu, Observatoire de Paris, Sorbonne Paris Cité, F-75205 Paris Cedex 13, France*
[35]*Wigner RCP, RMKI, H-1121 Budapest, Konkoly Thege Miklós út 29-33, Hungary*
[36]*Columbia University, New York, New York 10027, USA*
[37]*Stanford University, Stanford, California 94305, USA*
[38]*Università di Padova, Dipartimento di Fisica e Astronomia, I-35131 Padova, Italy*
[39]*INFN, Sezione di Padova, I-35131 Padova, Italy*
[40]*CAMK-PAN, 00-716 Warsaw, Poland*
[41]*Astronomical Observatory Warsaw University, 00-478 Warsaw, Poland*
[42]*University of Birmingham, Birmingham B15 2TT, United Kingdom*
[43]*Università degli Studi di Genova, I-16146 Genova, Italy*

[44]*INFN, Sezione di Genova, I-16146 Genova, Italy*
[45]*RRCAT, Indore MP 452013, India*
[46]*Faculty of Physics, Lomonosov Moscow State University, Moscow 119991, Russia*
[47]*SUPA, University of the West of Scotland, Paisley PA1 2BE, United Kingdom*
[48]*University of Western Australia, Crawley, Western Australia 6009, Australia*
[49]*Department of Astrophysics/IMAPP, Radboud University Nijmegen, P.O. Box 9010, 6500 GL Nijmegen, Netherlands*
[50]*ARTEMIS, Université Côte d'Azur, CNRS and Observatoire de la Côte d'Azur, F-06304 Nice, France*
[51]*MTA Eötvös University, "Lendulet" Astrophysics Research Group, Budapest 1117, Hungary*
[52]*Institut de Physique de Rennes, CNRS, Université de Rennes 1, F-35042 Rennes, France*
[53]*Washington State University, Pullman, Washington 99164, USA*
[54]*Università degli Studi di Urbino "Carlo Bo," I-61029 Urbino, Italy*
[55]*INFN, Sezione di Firenze, I-50019 Sesto Fiorentino, Firenze, Italy*
[56]*University of Oregon, Eugene, Oregon 97403, USA*
[57]*Laboratoire Kastler Brossel, UPMC-Sorbonne Universités, CNRS, ENS-PSL Research University, Collège de France, F-75005 Paris, France*
[58]*VU University Amsterdam, 1081 HV Amsterdam, Netherlands*
[59]*University of Maryland, College Park, Maryland 20742, USA*
[60]*Center for Relativistic Astrophysics and School of Physics, Georgia Institute of Technology, Atlanta, Georgia 30332, USA*
[61]*Laboratoire des Matériaux Avancés (LMA), IN2P3/CNRS, Université de Lyon, F-69622 Villeurbanne, Lyon, France*
[62]*Universitat de les Illes Balears – IEEC, E-07122 Palma de Mallorca, Spain*
[63]*Università di Napoli "Federico II," Complesso Universitario di Monte S.Angelo, I-80126 Napoli, Italy*
[64]*NASA/Goddard Space Flight Center, Greenbelt, Maryland 20771, USA*
[65]*Canadian Institute for Theoretical Astrophysics, University of Toronto, Toronto, Ontario M5S 3H8, Canada*
[66]*Tsinghua University, Beijing 100084, China*
[67]*University of Michigan, Ann Arbor, Michigan 48109, USA*
[68]*Università di Roma Tor Vergata, I-00133 Roma, Italy*
[69]*INFN, Sezion e di Roma Tor Vergata, I-00133 Roma, Italy*
[70]*National Tsing Hua University, Hsinchu City 30013, Taiwan, Republic of China*
[71]*Charles Sturt University, Wagga Wagga, New South Wales 2678, Australia*
[72]*University of Chicago, Chicago, Illinois 60637, USA*
[73]*Caltech CaRT, Pasadena, California 91125, USA*
[74]*Korea Institute of Science and Technology Information, Daejeon 305-806, Korea*
[75]*Australian National University, Canberra, Australian Capital Territory 0200, Australia*
[76]*Carleton College, Northfield, Minnesota 55057, USA*
[77]*INFN, Gran Sasso Science Institute, I-67100 L'Aquila, Italy*
[78]*Università di Roma "La Sapienza," I-00185 Roma, Italy*
[79]*University of Brussels, Brussels 1050, Belgium*
[80]*Texas Tech University, Lubbock, Texas 79409, USA*
[81]*Cardiff University, Cardiff CF24 3AA, United Kingdom*
[82]*University of Minnesota, Minneapolis, Minnesota 55455, USA*
[83]*The University of Melbourne, Parkville, Victoria 3010, Australia*
[84]*The University of Texas Rio Grande Valley, Brownsville, Texas 78520, USA*
[85]*The University of Sheffield, Sheffield S10 2TN, United Kingdom*
[86]*Montclair State University, Montclair, New Jersey 07043, USA*
[87]*Università di Trento, Dipartimento di Fisica, I-38123 Povo, Trento, Italy*
[88]*INFN, Trento Institute for Fundamental Physics and Applications, I-38123 Povo, Trento, Italy*
[89]*The Pennsylvania State University, University Park, Pennsylvania 16802, USA*
[90]*University of Cambridge, Cambridge CB2 1TN, United Kingdom*
[91]*Indian Institute of Technology, Gandhinagar Ahmedabad Gujarat 382424, India*
[92]*Institute for Plasma Research, Bhat, Gandhinagar 382428, India*
[93]*University of Szeged, Dóm tér 9, Szeged 6720, Hungary*
[94]*Embry-Riddle Aeronautical University, Prescott, Arizona 86301, USA*
[95]*Tata Institute for Fundamental Research, Mumbai 400005, India*
[96]*American University, Washington, D.C. 20016, USA*
[97]*University of Massachusetts-Amherst, Amherst, Massachusetts 01003, USA*
[98]*University of Adelaide, Adelaide, South Australia 5005, Australia*

[99]West Virginia University, Morgantown, West Virginia 26506, USA
[100]University of Białystok, 15-424 Białystok, Poland
[101]SUPA, University of Strathclyde, Glasgow G1 1XQ, United Kingdom
[102]IISER-TVM, CET Campus, Trivandrum Kerala 695016, India
[103]Northwestern University, Evanston, Illinois 60208, USA
[104]Institute of Applied Physics, Nizhny Novgorod, 603950, Russia
[105]Pusan National University, Busan 609-735, Korea
[106]Hanyang University, Seoul 133-791, Korea
[107]NCBJ, 05-400 Świerk-Otwock, Poland
[108]IM-PAN, 00-956 Warsaw, Poland
[109]Rochester Institute of Technology, Rochester, New York 14623, USA
[110]Monash University, Victoria 3800, Australia
[111]Seoul National University, Seoul 151-742, Korea
[112]ESPCI, CNRS, F-75005 Paris, France
[113]Università di Camerino, Dipartimento di Fisica, I-62032 Camerino, Italy
[114]Southern University and A&M College, Baton Rouge, Louisiana 70813, USA
[115]College of William and Mary, Williamsburg, Virginia 23187, USA
[116]Instituto de Física Teórica, University Estadual Paulista/ICTP South American Institute for Fundamental Research, São Paulo, São Paulo 01140-070, Brazil
[117]IISER-Kolkata, Mohanpur, West Bengal 741252, India
[118]Rutherford Appleton Laboratory, HSIC, Chilton, Didcot, Oxon OX11 0QX, United Kingdom
[119]Whitman College, 280 Boyer Ave, Walla Walla, Washington 9936, USA
[120]National Institute for Mathematical Sciences, Daejeon 305-390, Korea
[121]Hobart and William Smith Colleges, Geneva, New York 14456, USA
[122]Institute of Astronomy, 65-265 Zielona Góra, Poland
[123]Andrews University, Berrien Springs, Michigan 49104, USA
[124]Università di Siena, I-53100 Siena, Italy
[125]Trinity University, San Antonio, Texas 78212, USA
[126]University of Washington, Seattle, Washington 98195, USA
[127]Abilene Christian University, Abilene, Texas 79699, USA

(Received 30 November 2015; published 12 February 2016)

We present the results of a search for long-duration gravitational wave transients in two sets of data collected by the LIGO Hanford and LIGO Livingston detectors between November 5, 2005 and September 30, 2007, and July 7, 2009 and October 20, 2010, with a total observational time of 283.0 days and 132.9 days, respectively. The search targets gravitational wave transients of duration 10–500 s in a frequency band of 40–1000 Hz, with minimal assumptions about the signal waveform, polarization, source direction, or time of occurrence. All candidate triggers were consistent with the expected background; as a result we set 90% confidence upper limits on the rate of long-duration gravitational wave transients for different types of gravitational wave signals. For signals from black hole accretion disk instabilities, we set upper limits on the source rate density between 3.4×10^{-5} and 9.4×10^{-4} $\mathrm{Mpc}^{-3}\,\mathrm{yr}^{-1}$ at 90% confidence. These are the first results from an all-sky search for unmodeled long-duration transient gravitational waves.

DOI: 10.1103/PhysRevD.93.042005

I. INTRODUCTION

The goal of the Laser Interferometer Gravitational-Wave Observatory (LIGO) [1] and the Virgo detectors [2] is to directly detect and study gravitational waves (GWs). The direct detection of GWs holds the promise of testing general relativity in the strong-field regime, of providing a new probe of objects such as black holes and neutron stars, and of uncovering unanticipated new astrophysics.

LIGO and Virgo have jointly acquired data that have been used to search for many types of GW signals: unmodeled bursts of short duration (<1 s) [3–7], well-modeled chirps emitted by binary systems of compact objects [8–12], continuous signals emitted by asymmetric neutron stars [13–20], as well as a stochastic background of GWs [21–24]. For a complete review, see Ref. [25]. While no GW sources have been observed by the first-generation network of detectors, first detections are expected with the next generation of ground-based detectors: advanced LIGO [26], advanced Virgo [27], and the cryogenic detector KAGRA [28]. It is expected that the advanced detectors,

*Deceased.
†publication@ligo.org; publication@ego-gw.it

operating at design sensitivity, will be capable of detecting approximately 40 neutron star binary coalescences per year, although significant uncertainties exist [29].

Previous searches for unmodeled bursts of GWs [3–5] targeted source objects such as core-collapse supernovae [30], neutron-star-to-black-hole collapse [31], cosmic string cusps [32], binary black hole mergers [33–35], star-quakes in magnetars [36], pulsar glitches [37], and signals associated with gamma-ray bursts (GRBs) [38]. These burst searches typically look for signals of duration 1 s or shorter.

At the other end of the spectrum, searches for persistent, unmodeled (stochastic) GW backgrounds have also been conducted, including isotropic [21], anisotropic and point-source backgrounds [22]. This leaves the parameter space of unmodeled transient GWs not fully explored; indeed, multiple proposed astrophysical scenarios predict long-duration GW transients lasting from a few seconds to hundreds of seconds, or even longer, as described in Sec. II. The first search for unmodeled long-duration GW transients was conducted using LIGO data from the S5 science run, in association with long GRBs [39]. In this paper, we apply a similar technique [40] in order to search for long-lasting transient GW signals over all sky directions and for all times. We utilize LIGO data from the LIGO Hanford and Livingston detectors from the S5 and S6 science runs, lasting from November 5, 2005 to September 30, 2007 and from July 7, 2009 to October 20, 2010, respectively.

The organization of the paper is as follows: In Sec. II, we summarize different types of long-duration transient signals which may be observable by LIGO and Virgo. In Sec. III, we describe the selection of the LIGO S5 and S6 science run data that have been used for this study. We discuss the search algorithm, background estimation, and data quality methods in Sec. IV. In Sec. V, we evaluate the sensitivity of the search to simulated GW waveforms. The results of the search are presented in Sec. VI. We conclude with possible improvements for a long-transient GW search using data from the advanced LIGO and Virgo detectors in Sec. VII.

II. ASTROPHYSICAL SOURCES OF LONG GW TRANSIENTS

Some of the most compelling astrophysical sources of long GW transients are associated with extremely complex dynamics and hydrodynamic instabilities following the collapse of a massive star's core in the context of core-collapse supernovae and long GRBs [30,40,41]. Soon after core collapse and the formation of a protoneutron star, convective and other fluid instabilities (including standing accretion shock instability [42]) may develop behind the supernova shock wave as it transitions into an accretion shock. In progenitor stars with rapidly rotating cores, long-lasting, nonaxisymmetric rotational instabilities can be triggered by corotation modes [43–46]. Long-duration GW signals are expected from these violently aspherical dynamics, following within tens of milliseconds of the short-duration GW burst signal from core bounce and protoneutron star formation. Given the turbulent and chaotic nature of postbounce fluid dynamics, one expects a stochastic GW signal that could last from a fraction of a second to multiple seconds, and possibly even longer [30,40,47–50].

After the launch of an at least initially successful explosion, fallback accretion onto the newborn neutron star may spin it up, leading to nonaxisymmetric deformation and a characteristic upward chirp signal (700 Hz–few kHz) as the spin frequency of the neutron star increases over tens to hundreds of seconds [51,52]. GW emission may eventually terminate when the neutron star collapses to a black hole. The collapse process and formation of the black hole itself will also produce a short-duration GW burst [53,54].

In the collapsar model for long GRBs [55], a stellar-mass black hole forms, surrounded by a massive, self-gravitating accretion disk. This disk may be susceptible to various nonaxisymmetric hydrodynamic and magnetohydrodynamic instabilities which may lead to fragmentation and inspiral of fragments into the central black hole (e.g., Refs. [56,57]). In an extreme scenario of such accretion disk instabilities (ADIs), magnetically "suspended accretion" is thought to extract spin energy from the black hole and dissipate it via GW emission from nonaxisymmetric disk modes and fragments [58,59]. The associated GW signal is potentially long lasting (10–100 s) and predicted to exhibit a characteristic downward chirp.

Finally, in magnetar models for long and short GRBs (e.g., Refs. [60,61]), a long-lasting post-GRB GW transient may be emitted by a magnetar undergoing rotational or magnetic nonaxisymmetric deformation (e.g., Refs. [62,63]).

III. DATA SELECTION

During the fifth LIGO science run (S5, November 5, 2005 to September 30, 2007), the 4 km and 2 km detectors at Hanford, Washington (H1 and H2), and the 4 km detector at Livingston, Louisiana (L1), recorded data for nearly two years. They were joined on May 18, 2007 by the Virgo detector (V1) in Pisa, Italy, which was beginning its first science run. After a two-year period of upgrades to the detectors and the decommissioning of H2, the sixth LIGO and second and third Virgo scientific runs were organized jointly from July 7, 2009 to October 10, 2010.

Among the four detectors, H1 and L1 achieved the best strain sensitivity, reaching $\approx 2 \times 10^{-23}/\sqrt{\text{Hz}}$ around 150 Hz in 2010 [64,65]. Because of its reduced arm length, H2 sensitivity was at least a factor of 2 lower than H1 on average. V1 sensitivity varied over time, but was always lower than the sensitivity of H1 and L1 by a factor between

1.5 and 5 at frequencies higher than 60 Hz. Moreover, the H1-L1 pair live time was at least a factor 2 longer than the live time of the H1-V1 and L1-V1 pairs added together. Using Virgo data, however, could help with sky localization of source candidates; unfortunately, the sky localization was not implemented at the time of this search. Consequently, including Virgo data in this analysis would have increased the overall search sensitivity by only a few percent or less at the cost of analyzing two additional pairs of detectors. As a result, we have analyzed only S5 and S6 data from the H1-L1 pair for this search.

In terms of frequency content, we restrict the analysis to the 40–1000 Hz band. The lower limit is constrained by seismic noise, which steeply increases at lower frequencies in LIGO data. The upper limit is set to include the most likely regions of frequency space for long-transient GWs, while keeping the computational requirements of the search at an acceptable level. We note that the frequency range of our analysis includes the most sensitive band of the LIGO detectors, namely 100–200 Hz.

Occasionally, the detectors are affected by instrumental problems (data acquisition failures, misalignment of optical cavities, etc.) or environmental conditions (bad weather, seismic motion, etc.) that decrease their sensitivity and increase the rate of data artifacts, or glitches. Most of these periods have been identified and can be discarded from the analysis using data quality flags [66–69]. These are classified by each search into different categories depending on how the GW search is affected.

Category 1 data quality flags are used to define periods when the data should not be searched for GW signals because of serious problems, like invalid calibration. To search for GW signals, the interferometers should be locked and there should be no evidence of environmental noise transients corrupting the measured signal. For this search, we have used the category 1 data quality flags used by searches for an isotropic stochastic background of GWs [21,23]. This list of flags is almost identical to what has been used by the unmodeled all-sky searches for short-duration GW transients [3,4]. We also discard times when simulated signals are injected into the detectors through the application of a differential force onto the mirrors.

Category 2 data quality flags are used to discard triggers which pass all selection cuts in a search, but are clearly associated with a detector malfunction or an environmental condition [68]. In Sec. IV C, we explain which category 2 flags have been selected and how we use them in this search.

Overall, we discard 5.8% and 2.2% of H1-L1 coincident data with our choices of category 1 data quality flags for S5 and S6, respectively. The remaining coincident strain time series are divided into 500 s intervals with 50% overlap. Intervals smaller than 500 s are not considered. For the H1-L1 pair, this results in a total observation time of 283.0 days during S5 and 132.9 days for S6.

IV. LONG TRANSIENT GW SEARCH PIPELINE

A. Search algorithm

The search algorithm we employ is based on the cross-correlation of data from two GW detectors, as described in Ref. [40]. This algorithm builds a frequency-time map (ft-map) of the cross power computed from the strain time series of two spatially separated detectors. A pattern recognition algorithm is then used to identify clusters of above-threshold pixels in the map, thereby defining candidate triggers. A similar algorithm has been used to search for long-lasting GW signals in coincidence with long GRBs in LIGO data [39]. Here we extend the method to carry out an untriggered (all-sky, all-time) search, considerably increasing the parameter space covered by previous searches.

Following Ref. [40], each 500 s interval of coincident data is divided into 50% overlapping, Hann-windowed, 1 s long segments. Strain data from each detector in the given 1 s segment are then Fourier transformed, allowing formation of ft-maps with a pixel size of $1\ \mathrm{s} \times 1\ \mathrm{Hz}$. An estimator for GW power can be formed [40]:

$$\hat{Y}(t;f;\hat{\Omega}) = \frac{2}{\mathcal{N}}\mathrm{Re}[Q_{IJ}(t;f;\hat{\Omega})\tilde{s}_I^{\star}(t;f)\tilde{s}_J(t;f)]. \quad (1)$$

Here t is the start time of the pixel, f is the frequency of the pixel, $\hat{\Omega}$ is the sky direction, $\mathcal{N}$ is a window normalization factor, and $\tilde{s}_I$ and $\tilde{s}_J$ are the discrete Fourier transforms of the strain data from GW detectors I and J. We use the LIGO H1 and L1 detectors as the I and J detectors, respectively. The optimal filter Q_{IJ} takes into account the phase delay due to the spatial separation of the two detectors, $\Delta\vec{x}_{IJ}$, and the direction-dependent efficiency of the detector pair, $\epsilon_{IJ}(t;\hat{\Omega})$:

$$Q_{IJ}(t;f;\hat{\Omega}) = \frac{e^{2\pi i f \Delta\vec{x}_{IJ}\cdot\hat{\Omega}/c}}{\epsilon_{IJ}(t;\hat{\Omega})}. \quad (2)$$

The pair efficiency is defined by

$$\epsilon_{IJ}(t;\hat{\Omega}) = \frac{1}{2}\sum_A F_I^A(t;\hat{\Omega})F_J^A(t;\hat{\Omega}), \quad (3)$$

where $F_I^A(t;\hat{\Omega})$ is the antenna factor for detector I and A is the polarization state of the incoming GW [40]. An estimator for the variance of the $\hat{Y}(t;f,\hat{\Omega})$ statistic is then given by

$$\hat{\sigma}_Y^2(t;f;\hat{\Omega}) = \frac{1}{2}|Q_{IJ}(t;f;\hat{\Omega})|^2 P_I^{\mathrm{adj}}(t;f)P_J^{\mathrm{adj}}(t;f), \quad (4)$$

where $P_I^{\mathrm{adj}}(t;f)$ is the average one-sided power spectrum for detector I, calculated by using the data in eight nonoverlapping segments on each side of time segment t [40]. We can then define the cross-correlation signal-to-noise ratio (SNR) in a single pixel, ρ:

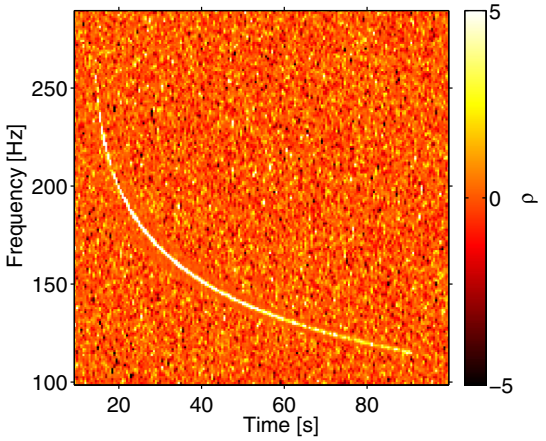


FIG. 1. ft-map of ρ (cross-correlation signal-to-noise ratio) using simulated Gaussian data. A simulated GW signal from an accretion disk instability [58,59] (model waveform ADI-E, see Table I) with known sky position is added to the data stream and is visible as a bright, narrow-band track. Blurring around the track is due to the usage of adjacent time segments in estimating $\hat{\sigma}_Y$; the estimate of $\hat{\sigma}_Y$ in these bins is affected by the presence of the GW signal.

$$\rho(t;f;\hat{\Omega}) = \hat{Y}(t;f;\hat{\Omega})/\hat{\sigma}_Y(t;f;\hat{\Omega}). \tag{5}$$

Because this is proportional to strain squared, it is an energy SNR, rather than an amplitude SNR.

This statistic is designed such that true GW signals should induce positive definite ρ when the correct filter is used (i.e., the sky direction $\hat{\Omega}$ is known). Consequently, using a wrong sky direction in the filter results in reduced or even negative ρ for real signals. Figure 1 shows an example ft-map of ρ containing a simulated GW signal with a known sky position.

Next, a seed-based clustering algorithm [70] is applied to the ρ ft-map to identify significant clusters of pixels. In particular, the clustering algorithm applies a threshold of $|\rho| \geq 1$ to identify seed pixels, and then groups these seed pixels that are located within a fixed distance (two pixels) of each other into a cluster. These parameters were determined through empirical testing with simulated long-transient GW signals similar to those used in this search (discussed further in Sec. V A). The resulting clusters (denoted Γ) are ranked using a weighted sum of the individual pixel values of $\hat{Y}$ and $\hat{\sigma}_Y$:

$$\mathrm{SNR}_\Gamma(\hat{\Omega}) = \frac{\sum_{t;f\in\Gamma} \hat{Y}(t;f;\hat{\Omega})\hat{\sigma}_Y^{-2}(t;f;\hat{\Omega})}{\left(\sum_{t;f\in\Gamma}\hat{\sigma}_Y^{-2}(t;f;\hat{\Omega})\right)^{1/2}}. \tag{6}$$

$\mathrm{SNR}_\Gamma(\hat{\Omega})$ represents the signal-to-noise ratio of the cluster Γ.

In principle, this pattern recognition algorithm could be applied for every sky direction $\hat{\Omega}$, since each sky direction is associated with a different filter $Q_{IJ}(t;f;\hat{\Omega})$. However, this procedure is prohibitively expensive from a computational standpoint. We have therefore modified the seed-based clustering algorithm to cluster both pixels with positive ρ and those with negative ρ (arising when an incorrect sky direction is used in the filter). Since the sky direction is not known in an all-sky search, this modification allows for the recovery of some of the power that would normally be lost due to a suboptimal choice of sky direction in the filter.

The algorithm is applied to each ft-map a certain number of times, each iteration corresponding to a different sky direction. The sky directions are chosen randomly, but are fixed for each stretch of uninterrupted science data. Different methods for choosing the sky directions were studied, including using only sky directions where the detector network had high sensitivity and choosing the set of sky directions to span the set of possible signal time delays. The results indicated that sky-direction choice did not have a significant impact on the sensitivity of the search.

We also studied the effect that the number of sky directions used had on the search sensitivity. We found that the search sensitivity increased approximately logarithmically with the number of sky directions, while the computational time increased linearly with the number of sky directions. The results of our empirical studies indicated that using five sky directions gave the optimal balance between computational time and search sensitivity.

This clustering strategy results in a loss of sensitivity of $\approx$10%–20% for the waveforms considered in this search as compared to a strategy using hundreds of sky directions and clustering only positive pixels. However, this strategy increases the computational speed of the search by a factor of 100 and is necessary to make the search computationally feasible.

We also apply two data-cleaning techniques concurrently with the data processing. First, we remove frequency bins that are known to be contaminated by instrumental and environmental effects. This includes the violin resonance modes of the suspensions, power line harmonics, and sinusoidal signals injected for calibration purposes. In total, we removed 47 1 Hz–wide frequency bins from the S5 data, and 64 1 Hz–wide frequency bins from the S6 data. Second, we require the waveforms observed by the two detectors to be consistent with each other, so as to suppress instrumental artifacts (glitches) that affect only one of the detectors. This is achieved by the use of a consistency-check algorithm [71] which compares the power spectra from each detector, taking into account the antenna factors.

B. Background estimation

An important aspect of any GW search is understanding the background of accidental triggers due to detector noise; this is crucial for preventing false identification of noise triggers as GW candidates. To estimate the false alarm rate (FAR), i.e. the rate of accidental triggers due to detector

noise, we introduce a nonphysical time shift between the H1 and L1 strain data before computing ρ. Analysis of the time-shifted data proceeds identically to that of unshifted data (see Sec. IV A for more details). With this technique, and assuming the number of hypothetical GW signals is small, the data should not contain a correlated GW signal, so any triggers will be generated by the detector noise. We repeat this process for multiple time shifts in order to gain a more accurate estimate of the FAR from detector noise.

As described in Sec. III, each analysis segment is divided into 500 s–long intervals which overlap by 50% and span the entire data set. For a given time shift i, the H1 data from interval n are correlated with L1 data from the interval $n + i$. Since the time gap between two consecutive intervals may be nonzero, the actual time shift applied in this process is at least $500 \times i$ seconds. The time shift is also circular: if for a time shift i, $n + i > N$ (where N is the number of overlapping intervals required to span the data set), then H1 data from the interval n are correlated with L1 data from the interval $n + i - N$. It is important to note that the minimum time-shift duration is much longer than the light travel time between the two detectors and also longer than the signal models we consider (see Sec. V for more information) in order to prevent accidental correlations.

Using this method, 100 time shifts have been processed to estimate the background during S5, amounting to a total analyzed live time of 84.1 years. We have also studied 100 time shifts of S6 data, with a total analyzed live time of 38.7 years. The cumulative rates of background triggers for the S5 and S6 data sets can be seen in Figs. 2 and 3, respectively.

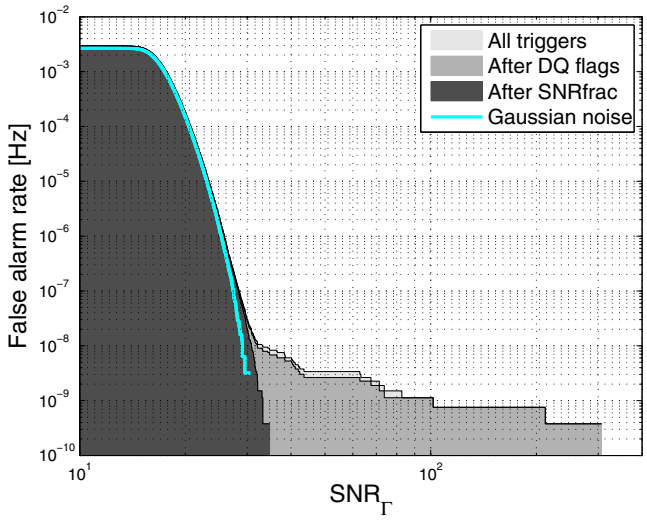


FIG. 2. The false alarm rate is shown as a function of the trigger SNR_Γ, for 100 time shifts of data from the S5 science run. Distributions are shown before and after applying the postprocessing cuts. Here, SNRfrac refers to a postprocessing cut based on how a trigger's power is distributed in time (described further in Sec. IV C). Also shown is the FAR distribution generated by a Monte Carlo simulation assuming Gaussian detector noise. Recall that this is an energy SNR, rather than an amplitude SNR.

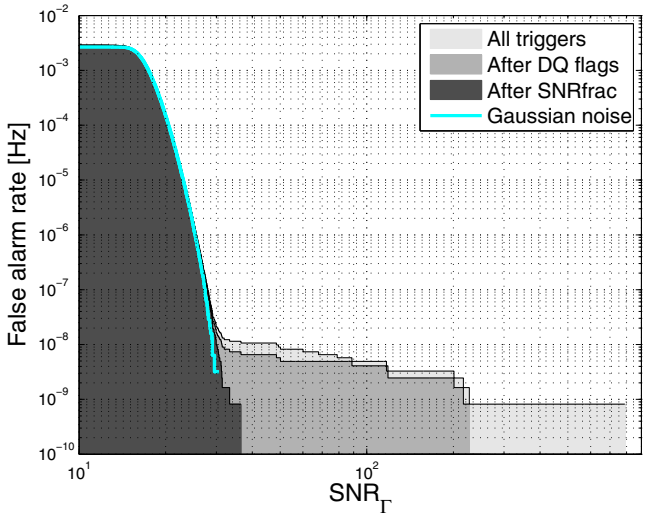


FIG. 3. The false alarm rate is shown as a function of the trigger signal-to-noise ratio, SNR_Γ, for 100 time shifts of data from the S6 science run. See caption of Fig. 2 for all details.

C. Rejection of loud noise triggers

As shown in Figs. 2 and 3, the background FAR distribution has a long tail extending to $\mathrm{SNR}_\Gamma > 100$; this implies that detector noise alone can generate triggers containing significant power. Many of these triggers are caused by short bursts of nonstationary noise (glitches) in H1 and/or L1, which randomly coincide during the time-shifting procedure. It is important to suppress these types of triggers so as to improve the significance of true GW signals in the unshifted data.

These glitches are typically much less than 1 s in duration, and as a result, nearly all of their power is concentrated in a single 1 s segment. To suppress these glitches, we have defined a discriminant variable, SNRfrac, that measures the fraction of SNR_Γ located in a single time segment. The same SNRfrac threshold of 0.45 was found to be optimal for all simulated GW waveforms using both S5 and S6 data. This threshold was determined by maximizing the search sensitivity for a set of simulated GW signals (see Sec. V); we note that this was done before examining the unshifted data, using only time-shifted triggers and simulated GW signals. The detection efficiency is minimally affected (less than 1%) by this SNRfrac threshold choice.

We also utilize LIGO data quality flags to veto triggers generated by a clearly identified source of noise. We have considered all category 2 data quality flags used in unmodeled or modeled transient GW searches [68]. These flags were defined using a variety of environmental monitors (microphones, seismometers, magnetometers, etc.) and interferometer control signals to identify stretches of data which may be compromised due to local environmental effects or instrumental malfunction. Since many of these data quality flags are not useful for rejecting noise triggers in this analysis, we select a set of effective data

quality flags by estimating the statistical significance of the coincidence between these data quality flags and the 100 loudest triggers from the time-shifted background study (no SNRfrac selection applied). The significance is defined by comparing the number of coincident triggers with the accidental coincidence mean and standard deviation. Given the small number of triggers we are considering (100), and in order to avoid accidental coincidence, we have applied a stringent selection: only those data quality flags which have a statistical significance higher than 12 standard deviations (as defined above) and an efficiency-over-dead-time ratio larger than 8 have been selected. Here, efficiency refers to the fraction of noise triggers flagged, while dead time is the amount of science data excluded by the flag.

For both the S5 and S6 data sets, this procedure selected data quality flags which relate to malfunctions of the longitudinal control of the Fabry-Perot cavities and those which indicate an increase in seismic noise. The total dead time which results from applying these data quality (DQ) flags amounts to ≈12 hours in H1 and L1 (0.18%) for S5, and ≈4 hours in H1 (0.13%) and ≈7 hours in L1 (0.22%) for S6.

As shown in Figs. 2 and 3, these two data quality cuts (SNRfrac and DQ flags) are useful for suppressing the high-SNR_Γ tail of the FAR distribution. More precisely, the SNRfrac cut is very effective for cleaning up coincident glitches with high SNR_Γ, while the DQ flags are capable of removing less extreme triggers occurring due to the presence of a well-identified noise source. We have thus decided to look at the unshifted (zero-lag) triggers after the SNRfrac cut is applied and to reserve the DQ flags for the exclusion of potential GW candidates that are actually due to a well-understood instrumental problem.

After the application of the SNRfrac cut, the resulting FAR distribution can be compared with that of a Monte Carlo simulation using a Gaussian noise distribution (assuming an initial LIGO noise sensitivity curve). A discrepancy of ≈10% in the total number of triggers and a slight excess of loud triggers are observed for both the S5 and S6 data sets when compared to Gaussian noise.

V. SEARCH SENSITIVITY

A. GW signal models

To assess the sensitivity of our search to realistic GW signals, we use 15 types of simulated GW signals. Four of these waveforms are based on an astrophysical model of a black hole accretion disk instability [58,59]. The other 11 waveforms are not based on a model of an astrophysical GW source, but are chosen to encapsulate various characteristics that long-transient GW signals may possess, including duration, frequency content, bandwidth, and rate of change of frequency. These *ad hoc* waveforms can be divided into three families: sinusoids with a time-dependent frequency content, sine-Gaussians, and band-limited white noise bursts. All waveforms have 1 s–long Hann-like tapers applied to the beginning and end of the waveforms in order to prevent data artifacts which may occur when the simulated signals have high intensity. In this section, we give a brief description of each type of GW signal model.

1. Accretion disk instabilities

In this study, we include four variations on the ADI model (see Sec. II for more details). Although this set of waveforms does not span the entire parameter space of the ADI model, it does encapsulate most of the possible variations in the signal morphology in terms of signal durations, frequency ranges and derivatives, and amplitudes (see Table I for a summary of the waveforms). While these waveforms may not be precise representations of realistic signals, they capture the salient features of many proposed models and produce long-lived spectrogram tracks.

2. Sinusoids

The sinusoidal waveforms are characterized by a sine function with a time-dependent frequency content. The waveforms are described by

$$h_+(t) = \frac{1+\cos^2\iota}{2}\cos 2\psi \cos\phi(t) - \cos\iota \sin 2\psi \sin\phi(t), \tag{7}$$

$$h_\times(t) = \frac{1+\cos^2\iota}{2}\sin 2\psi \cos\phi(t) + \cos\iota \cos 2\psi \sin\phi(t), \tag{8}$$

where ι is the inclination angle of the source, ψ is the source polarization, and $\phi(t)$ is a phase time series, given by

$$\phi(t) = 2\pi\left(f_0 t + \frac{1}{2}\left(\frac{df}{dt}\right)t^2 + \frac{1}{6}\left(\frac{d^2f}{dt^2}\right)t^3\right). \tag{9}$$

Two of the waveforms are completely monochromatic, two have a linear frequency dependence on time, and two

TABLE I. List of ADI waveforms [58,59] used to test the sensitivity of the search. Here, M is the mass of the central black hole, a^* is the dimensionless Kerr spin parameter of the black hole, and ϵ is the fraction of the disk mass that forms clumps. Frequency refers to the ending and starting frequencies of the GW signal, in that order. All waveforms have an accretion disk mass of 1.5 $M_\odot$.

Waveform	$M[M_\odot]$	a^*	ϵ	Duration [s]	Frequency [Hz]
ADI-A	5	0.30	0.050	39	135–166
ADI-B	10	0.95	0.200	9	110–209
ADI-C	10	0.95	0.040	236	130–251
ADI-E	8	0.99	0.065	76	111–234

TABLE II. List of sinusoidal waveforms used to test the sensitivity of the search. Here, f_0 is the initial frequency of the signal, df/dt is the frequency derivative, and d^2f/dt^2 is the second derivative of the frequency.

Waveform	Duration [s]	f_0 [Hz]	$\frac{df}{dt}$ [Hz/s]	$\frac{d^2f}{dt^2}$ [Hz/s^2]
MONO-A	150	90	0.0	0.00
MONO-B	250	505	0.0	0.00
LINE-A	250	50	0.6	0.00
LINE-B	100	900	−2.0	0.00
QUAD-A	30	50	0.0	0.33
QUAD-B	70	500	0.0	0.04

have a quadratic frequency dependence on time. This family of waveforms is summarized in Table II.

3. Sine-Gaussians

The sine-Gaussian waveforms are essentially monochromatic signals (see Eqs. (7) and (8)) multiplied by a Gaussian envelope:

$$e^{-t^2/\tau^2}. \tag{10}$$

Here, τ is the decay time, which defines the width of the Gaussian envelope. This set of waveforms is summarized in Table III.

4. Band-limited white noise bursts

We have generated white noise and used a sixth-order Butterworth band-pass filter to restrict the noise to the desired frequency band. Each polarization component of the simulated waveforms is generated independently; thus, the two components are uncorrelated. This family of waveforms is summarized in Table IV.

B. Sensitivity study

Using the waveforms described in the previous section, we performed a sensitivity study to determine the overall detection efficiency of the search as a function of waveform amplitude. First, for each of the 15 models, we generated 1500 injection times randomly between the beginning and the end of each of the two data sets, such that the injected waveform was fully included in a group of at least one 500 second–long analysis window. A minimal time lapse of 1000 s between two injections was enforced. For each of the 1500 injection times, we generated a simulated signal with random sky position, source inclination, and waveform polarization angle. The time-shifted data plus simulated signal was then analyzed using the search algorithm described in Sec. IV. The simulated signal was considered recovered if the search algorithm found a trigger fulfilling the following requirements:

(1) The trigger was found between the known start and end times of the simulated signal.
(2) The trigger was found within the known frequency band of the signal.
(3) The SNR_Γ of the trigger exceeded a threshold determined by the loudest trigger found in each data set (using the unshifted data).

This was repeated with 16 different signal amplitudes (logarithmically spaced) for each waveform and injection time in order to fully characterize the search's detection efficiency as a function of signal strength.

In Fig. 4, we show the efficiency, or ratio of recovered signals to the total number of simulations, as a function of either the distance to the source or the root-sum-squared strain amplitude (h_{rss}) arriving at the Earth, defined as

$$h_{\mathrm{rss}} = \sqrt{\int (|h_+(t)|^2 + |h_\times(t)|^2)dt}. \tag{11}$$

Among each family of waveforms, the pipeline efficiency has a frequency dependence that follows the data strain sensitivity of the detectors. The duration of the signal also plays a role, but to a lesser extent. We also note that the search efficiency for monochromatic waveforms (MONO and SG) is significantly worse than for the other waveforms. This is due to the usage of adjacent time segments to compute $\hat{\sigma}_Y$ (see Eq. (4)), which is affected by the presence of the GW signal.

TABLE III. List of sine-Gaussian waveforms used to test the sensitivity of the search. Here, τ is the decay time of the Gaussian envelope.

Waveform	Duration [s]	f_0 [Hz]	τ [s]
SG-A	150	90	30
SG-B	250	505	50

TABLE IV. List of band-limited white noise burst waveforms used to test the sensitivity of the search.

Waveform	Duration [s]	Frequency band [Hz]
WNB-A	20	50–400
WNB-B	60	300–350
WNB-C	100	700–750

VI. RESULTS

Having studied the background triggers and optimized the SNRfrac threshold using both background and simulated signals, the final step in the analysis is to apply the search algorithm to the unshifted (zero-lag) data (i.e. zero time shift between the H1 and L1 strain time series) in order to search for GW candidates. The resulting distributions of SNR_Γ for the zero-lag S5 and S6 data sets are compared to the corresponding background trigger distributions in Fig. 5. A slight deficit of triggers is present in the S6 zero

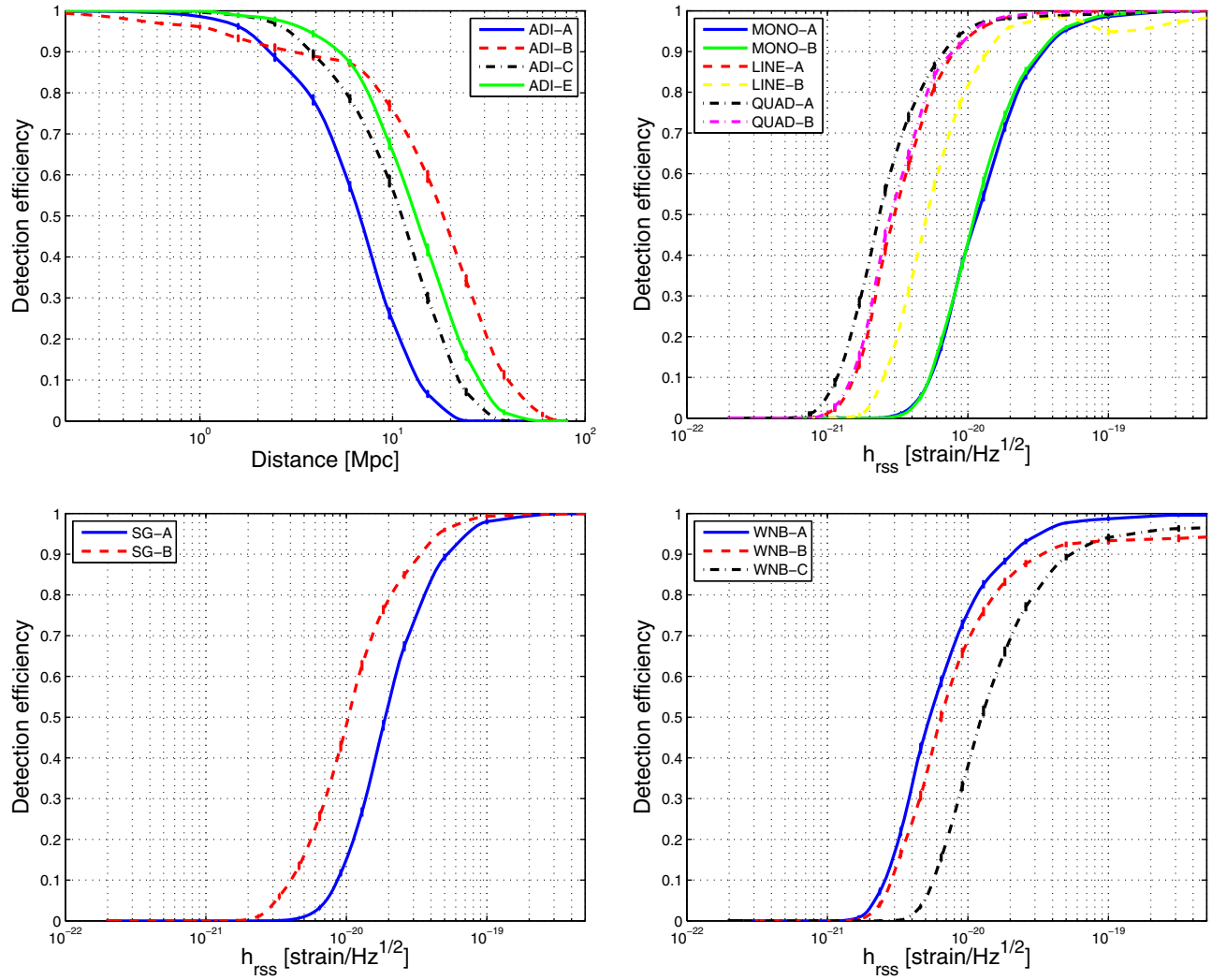


FIG. 4. Efficiency of the search pipeline at recovering different waveforms as a function of the distance to the source (for ADI waveforms) or the signal strength $h_{\rm rss}$ (all others). All results shown here used data from the S6 science run. The SNRfrac threshold is set at 0.45, and the recovery threshold is set at $\mathrm{SNR}_\Gamma = 27.13$. The error bars are computed using binomial statistics. Top left: ADI waveforms. Top right: sinusoidal waveforms. Bottom left: sine-Gaussian waveforms. Bottom right: white noise burst waveforms.

lag, but it remains within one standard deviation of what is expected from the background.

A. Loudest triggers

Here, we consider the most significant triggers from the S5 and S6 zero-lag analyses. We check the FAR of each trigger, which is the number of background triggers with SNR_Γ larger than a given threshold $\mathrm{SNR}^\star_\Gamma$ divided by the total background live time, $T_{\rm bkg}$. We also consider the false alarm probability (FAP), or the probability of observing at least N background triggers with SNR_Γ higher than $\mathrm{SNR}^\star_\Gamma$:

$$\mathrm{FAP}(N) = 1 - \sum_{n=0}^{n=N-1} \frac{\mu_{\rm bkg}^n}{n!} \times e^{-\mu_{\rm bkg}}, \qquad (12)$$

where $\mu_{\rm bkg}$ is the number of background triggers expected from a Poisson process (given by $\mu_{\rm bkg} = T_{\rm obs} \times \mathrm{FAR}(\mathrm{SNR}^\star_\Gamma)$, where $T_{\rm obs}$ is the observation time). For the loudest triggers in each data set, we take $N = 1$ to estimate the FAP.

The most significant triggers from the S5 and S6 zero-lag analyses occurred with false alarm probabilities of 54% and 92%, respectively. They have respective false alarm rates of 1.00 yr^{-1} and 6.94 yr^{-1}. This shows that triggers of this significance are frequently generated by detector noise alone, and thus, these triggers cannot be considered GW candidates.

Additional follow-up indicated that no category 2 data quality flags in H1 nor L1 were active at the time of these triggers. The examination of the ft-maps, the whitened time series around the time of the triggers, and the monitoring records indicate that these triggers were due to a small excess of noise in H1 and/or L1, and are not associated with a well-identified source of noise.

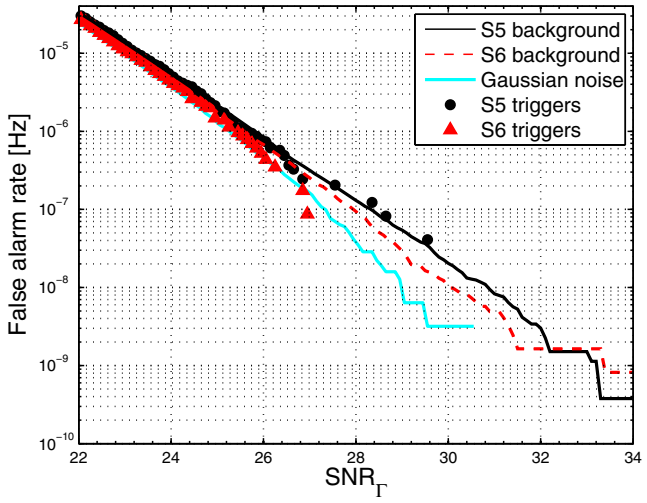


FIG. 5. FAR distribution of unshifted triggers from S5 (black circles) and S6 (red triangles) as a function of the trigger signal-to-noise ratio, SNR_Γ. The distributions are compared to the estimated background distributions for the S5 (solid black) and S6 (dashed red) data sets. We observe a slight deficit of triggers in S6 that remains within one standard deviation of what is expected from the time-shifted triggers. Also shown is the FAR distribution generated by a Monte Carlo simulation assuming Gaussian detector noise (solid cyan).

More information about these triggers is provided in Table V.

B. Rate upper limits

Since no GW candidates were identified, we proceed to place upper limits on the rate of long-duration GW transients assuming an isotropic and uniform distribution of sources. We use two implementations of the loudest event statistic [72] to set upper limits at 90% confidence. The first method uses the false alarm density (FAD) formalism [6,10], which accounts for both the background detector noise and the sensitivity of the search to simulated GW signals. For each simulated signal model, one calculates the efficiency of the search as a function of source distance at a given threshold on SNR_Γ, then integrates the efficiency over volume to gain a measure of the volume of space which is accessible to the search (referred to as the visible volume). The threshold is given by the SNR_Γ of the "loudest event," or in this case, the trigger with the lowest FAD. The 90% confidence upper limits are calculated (following Ref. [72]) as

$$R_{90\%,\mathrm{VT}} = \frac{2.3}{\sum_k V_{\mathrm{vis},k}(\mathrm{FAD}^\star) \times T_{\mathrm{obs},k}}. \quad (13)$$

Here, the index k runs over data sets, $V_{\mathrm{vis},k}(\mathrm{FAD}^\star)$ is the visible volume of search k calculated at the FAD of the loudest zero-lag trigger ($\mathrm{FAD}^\star$), and $T_{\mathrm{obs},k}$ is the observation time, or zero-lag live time of search k. The factor of 2.3 in the numerator is the mean rate (for zero observed triggers) which should give a nonzero number of triggers 90% of the time; it can be calculated by solving Eq. (12) for μ_{bkg} with $N = 1$ and a FAP of 0.9 (i.e., $1 - e^{-\mu_{\mathrm{bkg}}} = 0.9$). The subscript VT indicates that these upper limits are in terms of number of observations per volume per time.

Due to the dependence of these rate upper limits on distance to the source, they cannot be calculated for the *ad hoc* waveforms without setting an arbitrary source distance. A full description of the FAD and visible volume formalism is given in Appendix A; in Table VI, we present these upper limits for the four ADI waveforms.

Statistical and systematic uncertainties are discussed further in Appendix A, but we note here that the dominant source of uncertainty is the amplitude calibration uncertainty of the detectors. During the S5 science run, the amplitude calibration uncertainty was measured to be 10.4% and 14.4% for the H1 and L1 detectors, respectively, in the 40–2000 Hz frequency band [73]. Summing these uncertainties in quadrature gives a total calibration uncertainty of 17.8% on the amplitude, and thus, an uncertainty of 53.4% on the visible volume. For S6, the amplitude calibration uncertainty was measured at 4.0% for H1 and 7.0% for L1 in the 40–2000 Hz band, resulting in a total calibration uncertainty of 8.1% on the amplitude and 24.2% on the visible volume [74]. These uncertainties are marginalized over using a Bayesian method discussed in Appendix B. The upper limits presented in Table VI are conservative and include these uncertainties.

TABLE V. The most significant triggers from the S5 and S6 data sets. GPS times given correspond to trigger start times; both triggers had durations of 23.5 seconds.

Data set	SNR_Γ	FAR [yr^{-1}]	FAP	GPS time	Freq. [Hz]
S5	29.65	1.00	0.54	851136555.0	129–201
S6	27.13	6.94	0.92	958158359.5	537–645

TABLE VI. Rate upper limits on ADI waveforms calculated with Eq. (13). The visible volume of each search is shown to illustrate relative search sensitivities. Uncertainties on the visible volumes are not included, but are primarily due to calibration uncertainty, and are 53% and 24% for all waveforms in S5 and S6, respectively. 1σ uncertainties on the upper limits are marginalized over using the Bayesian method described in Appendix B.

	V_{vis}[Mpc^3]		
Waveform	S5	S6	$R_{90\%,\mathrm{VT}}$ [$\mathrm{Mpc}^{-3}\,\mathrm{yr}^{-1}$]
ADI-A	1.8×10^3	3.6×10^3	9.4×10^{-4}
ADI-B	5.7×10^4	9.1×10^4	3.4×10^{-5}
ADI-C	7.8×10^3	1.6×10^4	2.2×10^{-4}
ADI-E	1.6×10^4	3.2×10^4	1.1×10^{-4}

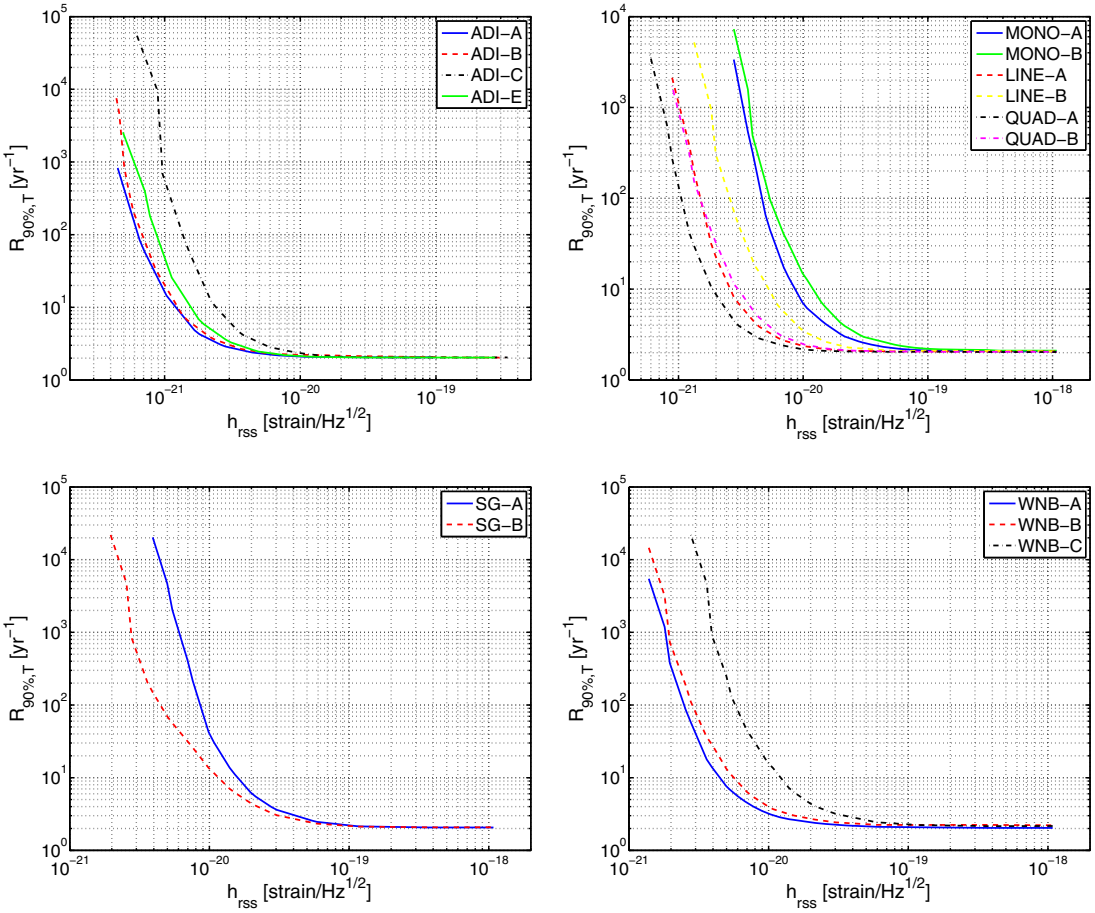


FIG. 6. Loudest event statistic upper limits for the 15 simulated GW signals used to test the sensitivity of the search (calculated with Eq. (14)). 1σ uncertainties are included by adjusting the signal amplitudes upward. Top left: ADI waveforms. Top right: sinusoidal waveforms. Bottom left: sine-Gaussian waveforms. Bottom right: white noise burst waveforms.

For signal models without a physical distance calibration, we use the loudest event statistic to calculate rate upper limits at 90% confidence based on the search pipeline's efficiency:

$$R_{90\%,\mathrm{T}} = \frac{2.3}{\sum_k \epsilon_k(\mathrm{SNR}^{\star}_{\Gamma,k}) T_{\mathrm{obs},k}}. \tag{14}$$

Here, ϵ_k is the efficiency of search k at a detection threshold $\mathrm{SNR}^{\star}_{\Gamma,k}$ corresponding to the loudest zero-lag trigger from search k. The resulting upper limits are in terms of the number of observations per time, as indicated by the subscript T. They are a function of signal strength in the form of root-sum-squared strain, h_{rss}, and are presented in Fig. 6.

Again, systematic uncertainty in the form of amplitude calibration uncertainty is the main source of uncertainty for these upper limits. This uncertainty is accounted for by adjusting the signal amplitudes used in the sensitivity study (and shown in the efficiency curves in Fig. 4) upward by a multiplicative factor corresponding to the respective 1σ amplitude calibration uncertainty; this results in conservative upper limits.

In Fig. 7, we show the $R_{90\%,\mathrm{T}}$ upper limits in terms of source distance for the ADI waveforms. To compare these upper limits to the $R_{90\%,\mathrm{VT}}$ upper limits, one would integrate the inverse of the $R_{90\%,\mathrm{T}}$ curves (shown in Fig. 7) over volume to obtain an overall estimate of the signal rate. The two methods have been compared, and the results are consistent within ≈25% for all four of the ADI waveforms. Differences between the two methods arise from the usage of different trigger ranking statistics (FAD vs. SNR_{Γ}), and the fact that the uncertainties are handled differently in each case.

C. Discussion

Given the absence of detection candidates in the search, we have reported upper limits on the event rate for different GW signal families. Specifically, Fig. 6 shows that, along with signal morphology, both the frequency and the duration of a signal influence the search sensitivity. The h_{rss} values for a search efficiency of 50%

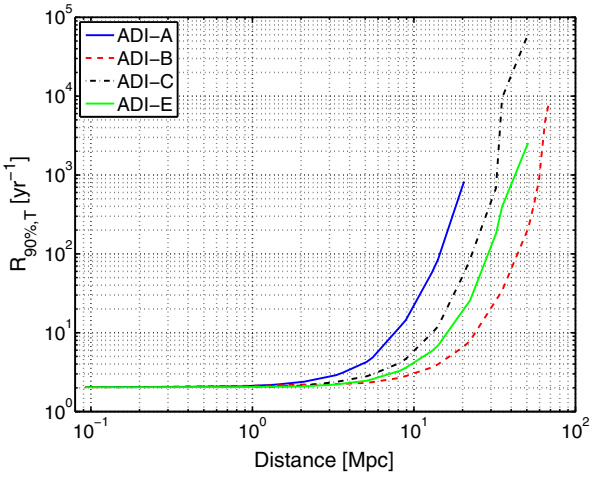


FIG. 7. Loudest event statistic upper limits for the four ADI waveforms used to test the sensitivity of the search. Here, the upper limits are plotted in terms of distance rather than $h_{\rm rss}$.

obtained with S5 and S6 data are reported in Table VII. For the ADI waveforms, the 50% efficiency distance is also given. Although these limits cannot be precisely compared to the results of unmodeled short transient GW searches [4] because different waveforms were used by the two searches, it is clear that in order for long transient GW signals to be observed, it is necessary for the source to be more energetic: the total energy radiated is spread over hundreds of seconds instead of a few hundred milliseconds.

One can also estimate the amount of energy emitted by a source located at a distance r where the search efficiency drops below 50% ($h_{\rm rss}^{50\%}$) using the quadrupolar radiation approximation to estimate the energy radiated by a pair of rotating point masses:

$$E_{\rm GW} \approx (h_{\rm rss}^{50\%})^2 r^2 \pi^2 f_{\rm GW}^2 \frac{c^3}{G}. \tag{15}$$

Considering the mean frequency of each GW waveform, we obtain an estimate of the energy that would have been released by a source that would be detected by this search. For the ADI waveforms, the corresponding energy is between $9 \times 10^{-8}\ {\rm M}_\odot c^2$ and $6 \times 10^{-7}\ {\rm M}_\odot c^2$. For the *ad hoc* waveforms, one must fix a fiducial distance at which one expects to observe a signal. For instance, considering a Galactic source at 10 kpc, the emitted energy would be in the range 2×10^{-7}–$2 \times 10^{-4}\ {\rm M}_\odot c^2$. This is still 2–4 orders of magnitude larger than the amount of energy estimated in Ref. [47] for a 10 kpc protoneutron star developing matter convection over 30 s: $4 \times 10^{-9}\ {\rm M}_\odot c^2$.

Finally, we note that the search for long-duration transient signals is also closely related to the effort by LIGO and Virgo to observe a stochastic background of GWs. One or more long-lived transient GW events, with a duration of days or longer, could produce an apparent signal in either the isotropic [21,23,24] or directional [22] stochastic GW searches. It was for this reason that this long-duration transient detection pipeline was originally developed [40]. The methods for detecting these long-duration transients have been adapted, in the study described in this present paper, to search for signals in the 10 s–to–500 s regime. A dedicated search for long-duration transient GW signals which last for days or longer will be a necessary component in the effort to understand the origin of apparent stochastic background signals which may be observed by LIGO and Virgo in the future [75].

TABLE VII. Values of $h_{\rm rss}$ and distance where the search achieves 50% efficiency for each of the simulated GW signals studied and each of the two data sets. $E_{\rm GW}$ is an estimate of the energy released (given by Eq. (15)) by a source located at the detection distance for the ADI waveforms, or at 10 kpc for the *ad hoc* waveforms.

Run	S5			S6		
Waveform	$h_{\rm rss}^{50\%}$ [Hz$^{-1/2}$]	distance$^{50\%}$ [Mpc]	$E_{\rm GW}$ [M$_\odot c^2$]	$h_{\rm rss}^{50\%}$ [Hz$^{-1/2}$]	distance$^{50\%}$ [Mpc]	$E_{\rm GW}$ [M$_\odot c^2$]
ADI-A	1.8×10^{-21}	5.4	1.5×10^{-7}	1.4×10^{-21}	6.8	9.4×10^{-8}
ADI-B	1.9×10^{-21}	16.3	1.9×10^{-7}	1.7×10^{-21}	18.6	1.5×10^{-7}
ADI-C	3.6×10^{-21}	8.9	9.9×10^{-7}	2.9×10^{-21}	11.3	6.3×10^{-7}
ADI-E	2.3×10^{-21}	11.5	3.3×10^{-7}	2.0×10^{-21}	13.4	2.4×10^{-7}
LINE-A	3.9×10^{-21}	…	4.9×10^{-7}	3.1×10^{-21}	…	3.1×10^{-7}
LINE-B	8.5×10^{-21}	…	9.6×10^{-5}	5.2×10^{-21}	…	3.7×10^{-5}
MONO-A	1.3×10^{-20}	…	3.1×10^{-6}	1.2×10^{-20}	…	2.4×10^{-6}
MONO-B	2.1×10^{-20}	…	2.3×10^{-4}	1.1×10^{-20}	…	7.0×10^{-5}
QUAD-A	2.7×10^{-21}	…	2.4×10^{-7}	2.4×10^{-21}	…	1.9×10^{-7}
QUAD-B	5.1×10^{-21}	…	1.6×10^{-5}	2.9×10^{-21}	…	5.3×10^{-6}
SG-A	2.4×10^{-20}	…	1.0×10^{-5}	1.9×10^{-20}	…	6.2×10^{-6}
SG-B	2.1×10^{-20}	…	2.5×10^{-4}	1.0×10^{-20}	…	5.9×10^{-5}
WNB-A	7.2×10^{-21}	…	5.5×10^{-6}	5.5×10^{-21}	…	3.2×10^{-6}
WNB-B	9.1×10^{-21}	…	1.8×10^{-5}	6.4×10^{-21}	…	9.2×10^{-6}
WNB-C	2.1×10^{-20}	…	5.0×10^{-4}	1.3×10^{-20}	…	1.7×10^{-4}

VII. CONCLUSIONS

In this paper, we have presented an all-sky search for long-lasting GW transients with durations between a few seconds and a few hundred seconds. We performed the search on data from the LIGO H1 and L1 detectors collected during the S5 and S6 science runs. We used a cross-correlation pipeline to analyze the data and identify potential GW candidate triggers. To reject high-SNR_Γ triggers due to detector noise, we defined a discriminant cut based on the trigger morphology. We have also used data quality flags that veto well-identified instrumental or environmental noise sources to remove significant outliers. No GW candidates were identified in this search, and as a consequence, we set upper limits on several types of simulated GW signals. These are the first upper limits from an unmodeled all-sky search for long-transient GWs. The upper limits are given in Table VI and Figs. 6 and 7.

After 2010, the LIGO and Virgo interferometers went through a series of upgrades [26,27]. LIGO has just started its first observational campaign with its advanced configuration and will be joined by Virgo in 2016 [29]. The strain sensitivity of the advanced detectors is expected to eventually reach a factor of 10 better than the first-generation detectors. This development alone should increase the distance reach of our search by a factor of 10, the energy sensitivity by a factor of 100, and the volume of space which we can probe by a factor of 1000.

Improvements are also being made to this search pipeline; a technique for generating triggers called "seedless clustering" has been shown to increase the sensitivity of the search by 50% or more in terms of distance [76–81]. The improvements to the search pipeline described in this paper, coupled with the increased sensitivity of LIGO and Virgo, will drastically improve the probability of detecting long-duration transient GWs and pave the way for an exciting future in GW astronomy.

ACKNOWLEDGMENTS

The authors gratefully acknowledge the support of the United States National Science Foundation (NSF) for the construction and operation of the LIGO Laboratory; the Science and Technology Facilities Council (STFC) of the United Kingdom, the Max-Planck-Society (MPS), and the State of Niedersachsen/Germany for support of the construction and operation of the GEO600 detector; and the Italian Istituto Nazionale di Fisica Nucleare (INFN) and the French Centre National de la Recherche Scientifique (CNRS) for the construction and operation of the Virgo detector and the creation and support of the EGO consortium. The authors also gratefully acknowledge research support from these agencies as well as by the Australian Research Council; the International Science Linkages program of the Commonwealth of Australia; the Council of Scientific and Industrial Research of India; the Department of Science and Technology, India; the Science & Engineering Research Board (SERB), India; the Ministry of Human Resource Development, India; the Spanish Ministerio de Economía y Competitividad; the Conselleria d'Economia i Competitivitat and Conselleria d'Educaci, Cultura i Universitats of the Govern de les Illes Balears; the Foundation for Fundamental Research on Matter supported by the Netherlands Organisation for Scientific Research; the National Science Centre of Poland; the European Union; the Royal Society; the Scottish Funding Council; the Scottish Universities Physics Alliance; the National Aeronautics and Space Administration; the Hungarian Scientific Research Fund (OTKA); the Lyon Institute of Origins (LIO); the National Research Foundation of Korea; Industry Canada and the Province of Ontario through the Ministry of Economic Development and Innovation; the Natural Science and Engineering Research Council, Canada; the Brazilian Ministry of Science, Technology, and Innovation; the Carnegie Trust; the Leverhulme Trust; the David and Lucile Packard Foundation; the Research Corporation; and the Alfred P. Sloan Foundation. The authors gratefully acknowledge the support of the NSF, STFC, MPS, INFN, CNRS and the State of Niedersachsen/Germany for provision of computational resources.

APPENDIX A: VISIBLE VOLUME AND FALSE ALARM DENSITY

In order to constrain the rate and source density of the GW signals studied in this search, we estimate the volume of the sky in which the search algorithm is sensitive to these signals. For this, we use the visible volume [6,10]

$$V_{\mathrm{vis}}(\mathrm{SNR}_\Gamma) = \sum_i 4\pi r_i^2 \left(\frac{dN_{\mathrm{inj}}}{dr}(r_i)\right)^{-1}. \quad \text{(A1)}$$

Here the index i runs over detected injections, r_i is the distance to the ith injection, and dN_{inj}/dr is the radial density of injections. The SNR_Γ parameter sets the threshold which determines whether an injection is recovered or not. To calculate the visible volume, we require distance-calibrated waveforms, so this method is not practical for the *ad hoc* waveforms discussed previously.

Our estimate of the visible volume is affected by both statistical and systematic uncertainties. We can estimate the statistical uncertainty on the visible volume using binomial statistics [6,10]:

$$\sigma_{\mathrm{stat}} = \sqrt{\sum_i \left[4\pi r_i^2 \left(\frac{dN_{\mathrm{inj}}}{dr}(r_i)\right)^{-1}\right]^2}. \quad \text{(A2)}$$

Systematic uncertainty on the visible volume comes from the amplitude calibration uncertainties of the detectors:

$$\sigma_{\rm sys} = 3 \times V_{\rm vis} \times \sigma_{\rm calibration}. \quad \text{(A3)}$$

These uncertainties are discussed further in Sec. VI B. We can estimate the total uncertainty on the visible volume by summing the statistical and systematic uncertainties in quadrature:

$$\sigma_{V_{\rm vis}} = \sqrt{\sigma^2_{\rm stat} + \sigma^2_{\rm sys}}. \quad \text{(A4)}$$

We note that the statistical uncertainty is negligible for this search compared to the systematic uncertainty from the amplitude calibration uncertainty of the detectors.

The false alarm density (FAD) statistic is useful for comparing the results of searches over different data sets or even using different detector networks [6,10,82]. It provides an estimate of the number of background triggers expected given the visible volume and background live time of the search. The classical FAD is defined in terms of the FAR divided by the visible volume:

$$\mathrm{FAD_c}(\mathrm{SNR}_\Gamma) = \frac{\mathrm{FAR}(\mathrm{SNR}_\Gamma)}{V_{\rm vis}(\mathrm{SNR}_\Gamma)}. \quad \text{(A5)}$$

In this way, the FAD accounts for the network sensitivity to GW sources as well as the detector noise level and the accumulated live time.

We follow Ref. [82] to define a FAD which produces a monotonic ranking of triggers:

$$\mathrm{FAD}(\mathrm{SNR}_{\Gamma,i}) = \min(\mathrm{FAD_c}(\mathrm{SNR}_{\Gamma,i}), \mathrm{FAD_c}(\mathrm{SNR}_{\Gamma,i-1})), \quad \text{(A6)}$$

where the index i runs over triggers in increasing order of SNR_Γ.

One then uses the FAD to combine results from searches over different data sets or with different detector networks by calculating the time-volume productivity of the combined search:

$$\nu(\mathrm{FAD}) = \sum_k V_{{\rm vis},k}(\mathrm{FAD}) \times T_{{\rm obs},k}. \quad \text{(A7)}$$

Here the index k runs over data sets or detector networks. We note that the denominator in Eq. (13) is equal to ν as described here. The uncertainty on ν can be calculated as

$$\sigma_\nu(\mathrm{FAD}) = \sqrt{\sum_k T^2_{{\rm obs},k} \sigma^2_{V_{{\rm vis},k}}(\mathrm{FAD})}. \quad \text{(A8)}$$

The combined time-volume product is then used to calculate final upper limits (see Eqs. (13) and (B1)).

APPENDIX B: BAYESIAN FORMALISM FOR FAD UPPER LIMIT CALCULATION

The observed astrophysical rate of triggers is given by

$$R = \frac{N}{\nu(\mathrm{FAD}^\star)}, \quad \text{(B1)}$$

where N is the number of triggers observed by the search, ν is the time-volume product described in Eq. (A7), and $\mathrm{FAD}^\star$ is the false alarm density of the most significant zero-lag trigger. Although this search found no GW candidates, N is Poisson distributed, with some underlying mean and variance μ. To properly handle the uncertainty associated with the time-volume product, we utilize a Bayesian formalism to account for uncertainties in both quantities in the calculation of rate upper limits. Here, our goal is to constrain the rate using the mean expected number of triggers, μ.

Given an observation of N triggers with a time-volume product of $\bar{\nu}$, we can define a posterior distribution for μ and ν in terms of Bayes' theorem:

$$P(\mu, \nu | N, \bar{\nu}) = \frac{P(N, \bar{\nu} | \mu, \nu) P(\mu, \nu)}{P(N, \bar{\nu})}, \quad \text{(B2)}$$

where $P(\mu, \nu | N, \bar{\nu})$ is the posterior distribution, $P(N, \bar{\nu} | \mu, \nu)$ is the likelihood, $P(\mu, \nu)$ are the priors, and $P(N, \bar{\nu})$ is the evidence.

We may disregard the evidence since it is simply a normalization factor, and use uniform priors on μ and ν:

$$\mu \in [0, \mu_{\rm max}], \quad \text{(B3a)}$$

$$\nu \in [0, \nu_{\rm max}]. \quad \text{(B3b)}$$

Here $\mu_{\rm max}$ and $\nu_{\rm max}$ are defined to be large enough that all of the significant posterior mass is enclosed.

The likelihood function can be framed as the product of two separate distributions: a Poisson distribution with mean μ and a Gaussian distribution with mean $\bar{\nu}$ and sigma σ_ν (see Eq. (A8)).

$$P(N, \bar{\nu} | \mu, \nu) = \frac{e^{-\mu} \mu^N}{N!} \frac{e^{-(\nu - \bar{\nu})^2/(2\sigma^2_{\bar{\nu}})}}{\sqrt{2\pi}\sigma_\nu}. \quad \text{(B4)}$$

Using this formalism, we can calculate the posterior distribution as a function of μ and ν. However, we are primarily interested in setting limits on the rate, given as the ratio of μ and ν. We can transform the posterior distribution to be a function of two new variables by multiplying the original posterior by the Jacobian determinant of the transformation:

$$P(R, \nu | N, \bar{\nu}) = P(\mu, \nu | N, \bar{\nu}) \times |J|. \quad \text{(B5)}$$

Choosing the new variables to be R and ν (for simplicity), we obtain a Jacobian determinant of

$$|J| = \left| \begin{matrix} \frac{\partial \mu}{\partial R} & \frac{\partial \mu}{\partial \nu} \\ \frac{\partial \nu}{\partial R} & \frac{\partial \nu}{\partial \nu} \end{matrix} \right| = \nu. \tag{B6}$$

This gives a posterior distribution of

$$P(R, \nu | N, \bar{\nu}) = \nu \frac{e^{-\mu} \mu^N}{N!} \frac{e^{-(\nu-\bar{\nu})^2/(2\sigma_\nu^2)}}{\sqrt{2\pi}\sigma_\nu}. \tag{B7}$$

Finally, we marginalize over ν to get the posterior distribution of R:

$$P(R|N, \bar{\nu}) = \int_0^{\nu_{\max}} P(R, \nu | N, \bar{\nu}) d\nu. \tag{B8}$$

Using this distribution, we can find the 90% limit on R, $R_{90\%,\mathrm{VT}}$, such that 90% of the posterior mass is enclosed, by numerically solving Eq. (B9):

$$0.9 = \int_0^{R_{90\%,\mathrm{VT}}} P(R|N, \bar{\nu}) dR. \tag{B9}$$

[1] B. Abbott *et al.* (LIGO Scientific Collaboration), Rep. Prog. Phys. **72**, 076901 (2009).
[2] T. Accadia *et al.* (Virgo Collaboration), J. Instrum. **7**, P03012 (2012).
[3] J. Abadie *et al.* (LIGO Scientific Collaboration and Virgo Collaboration), Phys. Rev. D **81**, 102001 (2010).
[4] J. Abadie *et al.* (LIGO Scientific Collaboration and Virgo Collaboration), Phys. Rev. D **85**, 122007 (2012).
[5] J. Aasi *et al.* (LIGO Scientific Collaboration and Virgo Collaboration), Phys. Rev. Lett. **112**, 131101 (2014).
[6] J. Abadie *et al.* (LIGO Scientific Collaboration and Virgo Collaboration), Phys. Rev. D **85**, 102004 (2012).
[7] J. Aasi *et al.* (LIGO Scientific Collaboration and Virgo Collaboration), Phys. Rev. D **89**, 122003 (2014).
[8] J. Abadie *et al.* (LIGO Scientific Collaboration and Virgo Collaboration), Phys. Rev. D **82**, 102001 (2010).
[9] J. Abadie *et al.* (LIGO Scientific Collaboration and Virgo Collaboration), Phys. Rev. D **85**, 082002 (2012).
[10] J. Abadie *et al.* (LIGO Scientific Collaboration and Virgo Collaboration), Phys. Rev. D **83**, 122005 (2011).
[11] J. Aasi *et al.* (LIGO Scientific Collaboration and Virgo Collaboration), Phys. Rev. D **87**, 022002 (2013).
[12] J. Aasi *et al.* (LIGO Scientific Collaboration and Virgo Collaboration), Phys. Rev. D **89**, 102006 (2014).
[13] B. Abbott *et al.* (LIGO Scientific Collaboration), Astrophys. J. **683**, L45 (2008).
[14] J. Aasi *et al.* (LIGO Scientific Collaboration and Virgo Collaboration), Phys. Rev. D **87**, 042001 (2013).
[15] J. Abadie *et al.* (LIGO Scientific Collaboration and Virgo Collaboration), Phys. Rev. D **85**, 022001 (2012).
[16] J. Aasi *et al.* (LIGO Scientific Collaboration and Virgo Collaboration), Astrophys. J. **785**, 119 (2014).
[17] J. Aasi *et al.* (LIGO Scientific Collaboration and Virgo Collaboration), Phys. Rev. D **88**, 102002 (2013).
[18] J. Aasi *et al.* (LIGO Scientific Collaboration and Virgo Collaboration), Phys. Rev. D **90**, 062010 (2014).
[19] J. Aasi *et al.* (LIGO Scientific Collaboration and Virgo Collaboration), Classical Quantum Gravity **31**, 085014 (2014).
[20] J. Aasi *et al.* (LIGO Scientific Collaboration and Virgo Collaboration), Classical Quantum Gravity **31**, 165014 (2014).
[21] B. Abbott *et al.* (LIGO Scientific Collaboration and Virgo Collaboration), Nature (London) **460**, 990 (2009).
[22] B. Abbott *et al.* (LIGO Scientific Collaboration and Virgo Collaboration), Phys. Rev. Lett. **107**, 271102 (2011).
[23] J. Aasi *et al.* (LIGO Scientific Collaboration and Virgo Collaboration), Phys. Rev. Lett. **113**, 231101 (2014).
[24] J. Aasi *et al.* (LIGO Scientific Collaboration and Virgo Collaboration), Phys. Rev. D **91**, 022003 (2015).
[25] M. A. Bizouard and M. A. Papa, C.R. Phys. **14**, 352 (2013).
[26] J. Aasi *et al.* (LIGO Scientific Collaboration), Classical Quantum Gravity **32**, 074001 (2015).
[27] F. Acernese *et al.* (Virgo Collaboration), Classical Quantum Gravity **32**, 024001 (2015).
[28] T. Uchiyama, K. Furuta, M. Ohashi, S. Miyoki, O. Miyakawa, and Y. Saito, Classical Quantum Gravity **31**, 224005 (2014).
[29] J. Aasi *et al.* (LIGO Scientific Collaboration and Virgo Collaboration), arXiv:1304.0670.
[30] C. D. Ott, Classical Quantum Gravity **26**, 063001 (2009).
[31] L. Baiotti, I. Hawke, and L. Rezzolla, Classical Quantum Gravity **24**, S187 (2007).
[32] T. Damour and A. Vilenkin, Phys. Rev. D **64**, 064008 (2001).
[33] K. Belczynski, A. Buonanno, M. Cantiello, C. L. Fryer, D. E. Holz, I. Mandel, M. C. Miller, and M. Walczak, Astrophys. J. **789**, 120 (2014).
[34] M. Shibata and K. Taniguchi, Living Rev. Relativity **14**, 6 (2011).
[35] Z. B. Etienne, J. A. Faber, Y. T. Liu, S. L. Shapiro, K. Taniguchi, and T. W. Baumgarte, Phys. Rev. D **77**, 084002 (2008).
[36] S. Mereghetti, Astron. Astrophys. Rev. **15**, 225 (2008).
[37] N. Andersson and G. L. Comer, Phys. Rev. Lett. **87**, 241101 (2001).
[38] M. Briggs *et al.* (LIGO Scientific Collaboration and Virgo Collaboration), Astrophys. J. **760**, 12 (2012).
[39] J. Aasi *et al.* (LIGO Scientific Collaboration and Virgo Collaboration), Phys. Rev. D **88**, 122004 (2013).
[40] E. Thrane, S. Kandhasamy, C. D. Ott, W. G. Anderson, N. L. Christensen *et al.*, Phys. Rev. D **83**, 083004 (2011).
[41] K. Kotake, C.R. Phys. **14**, 318 (2013).

[42] J. M. Blondin, A. Mezzacappa, and C. DeMarino, Astrophys. J. **584**, 971 (2003).
[43] C. D. Ott, S. Ou, J. E. Tohline, and A. Burrows, Astrophys. J. **625**, L119 (2005).
[44] C. D. Ott, H. Dimmelmeier, A. Marek, H.-T. Janka, I. Hawke, B. Zink, and E. Schnetter, Phys. Rev. Lett. **98**, 261101 (2007).
[45] S. Scheidegger, R. Käppeli, S. C. Whitehouse, T. Fischer, and M. Liebendörfer, Astron. Astrophys. **514**, A51 (2010).
[46] T. Kuroda, T. Takiwaki, and K. Kotake, Phys. Rev. D **89**, 044011 (2014).
[47] E. Mueller, M. Rampp, R. Buras, H. T. Janka, and D. H. Shoemaker, Astrophys. J. **603**, 221 (2004).
[48] K. Kotake, W. Iwakami, N. Ohnishi, and S. Yamada, Astrophys. J. **697**, L133 (2009).
[49] B. Müller, H.-T. Janka, and A. Marek, Astrophys. J. **766**, 43 (2013).
[50] K. N. Yakunin, A. Mezzacappa, P. Marronetti, S. Yoshida, S. W. Bruenn, W. R. Hix, E. J. Lentz, O. E. B. Messer, J. A. Harris, E. Endeve *et al.*, Phys. Rev. D **92**, 084040 (2015).
[51] A. L. Piro and C. D. Ott, Astrophys. J. **736**, 108 (2011).
[52] A. L. Piro and E. Thrane, Astrophys. J. **761**, 63 (2012).
[53] C. D. Ott, C. Reisswig, E. Schnetter, E. O'Connor, U. Sperhake, F. Löffler, P. Diener, E. Abdikamalov, I. Hawke, and A. Burrows, Phys. Rev. Lett. **106**, 161103 (2011).
[54] T. Dietrich and S. Bernuzzi, Phys. Rev. D **91**, 044039 (2015).
[55] S. E. Woosley, Astrophys. J. **405**, 273 (1993).
[56] A. L. Piro and E. Pfahl, Astrophys. J. Lett. **658**, 1173 (2007).
[57] K. Kiuchi, M. Shibata, P. J. Montero, and J. A. Font, Phys. Rev. Lett. **106**, 251102 (2011).
[58] M. H. P. M. van Putten, Phys. Rev. Lett. **87**, 091101 (2001).
[59] M. H. P. M. van Putten, A. Levinson, H. K. Lee, T. Regimbau, M. Punturo, and G. M. Harry, Phys. Rev. D **69**, 044007 (2004).
[60] B. Metzger, D. Giannios, T. Thompson, N. Bucciantini, and E. Quataert, Mon. Not. R. Astron. Soc. **413**, 2031 (2011).
[61] A. Rowlinson, P. T. O'Brien, B. D. Metzger, N. R. Tanvir, and A. J. Levan, Mon. Not. R. Astron. Soc. **430**, 1061 (2013).
[62] A. Corsi and P. Mészáros, Astrophys. J. **702**, 1171 (2009).
[63] L. Gualtieri, R. Ciolfi, and V. Ferrari, Classical Quantum Gravity **28**, 114014 (2011).
[64] J. Abadie *et al.* (LIGO Scientific Collaboration and Virgo Collaboration), LIGO Report No. T1100338.
[65] J. Abadie *et al.* (LIGO Scientific Collaboration and Virgo Collaboration), LIGO Report No. T0900499.
[66] N. Christensen (LIGO Scientific Collaboration and Virgo Collaboration), Classical Quantum Gravity **27**, 194010 (2010).
[67] J. Slutsky, L. Blackburn, D. Brown, L. Cadonati, J. Cain *et al.*, Classical Quantum Gravity **27**, 165023 (2010).
[68] J. Aasi *et al.* (LIGO Scientific Collaboration and Virgo Collaboration), Classical Quantum Gravity **32**, 115012 (2015).
[69] J. Aasi *et al.* (LIGO Scientific Collaboration and Virgo Collaboration), Classical Quantum Gravity **29**, 155002 (2012).
[70] T. Prestegard and E. Thrane, LIGO Report No. L1200204.
[71] T. Prestegard, E. Thrane, N. L. Christensen, M. W. Coughlin, B. Hubbert, S. Kandhasamy, E. MacAyeal, and V. Mandic, Classical Quantum Gravity **29**, 095018 (2012).
[72] R. Biswas, P. R. Brady, J. D. E. Creighton, and S. Fairhurst, Classical Quantum Gravity **26**, 175009 (2009).
[73] J. Abadie *et al.* (LIGO Scientific Collaboration), Nucl. Instrum. Methods Phys. Res., Sect. A **624**, 223 (2010).
[74] I. Bartos *et al.*, LIGO Report No. T1100071.
[75] E. Thrane, V. Mandic, and N. Christensen, Phys. Rev. D **91**, 104021 (2015).
[76] E. Thrane and M. Coughlin, Phys. Rev. D **88**, 083010 (2013).
[77] E. Thrane and M. Coughlin, Phys. Rev. D **89**, 063012 (2014).
[78] M. Coughlin, E. Thrane, and N. Christensen, Phys. Rev. D **90**, 083005 (2014).
[79] M. Coughlin, P. Meyers, E. Thrane, J. Luo, and N. Christensen, Phys. Rev. D **91**, 063004 (2015).
[80] M. Coughlin, P. Meyers, S. Kandhasamy, E. Thrane, and N. Christensen, Phys. Rev. D **92**, 043007 (2015).
[81] E. Thrane and M. Coughlin, Phys. Rev. Lett. **115**, 181102 (2015).
[82] S. Klimenko, C. Pankow, and G. Vedovato, LIGO Report No. L1300869.



https://dspace.org/

All-sky search for long-duration gravitational wave transients with initial LIGO

Abbott, B. P.; Davies, G. S.; LIGO Scientific Collaboration and Virgo Collaboration

2016-02-12
American Physical Society
http://dspace.lib.cranfield.ac.uk/handle/1826/11728
Abbott BP, et al., (LIGO Collaboration and Virgo Collaboration). (2016) All-sky search for long-duration gravitational wave transients with initial LIGO. Physical Review D, Volume 93, Issue 4, February 2016, Article Number 042005

Downloaded from a DSpace repository. https://dspace.org/